Biogeosciences, 22, 19–39, 2025
https://doi.org/10.5194/bg-22-19-2025

Biogeosciences Open Access EGU

No increase is detected and modeled for the seasonal cycle amplitude of $\delta^{13}C$ of atmospheric carbon dioxide

Fortunat Joos[1,2], **Sebastian Lienert**[1,2], **and Sönke Zaehle**[3]

[1]Climate and Environmental Physics, University of Bern, Bern, Switzerland
[2]Oeschger Centre for Climate Change Research, University of Bern, Bern, Switzerland
[3]Max Planck Institute for Biogeochemistry, P.O. Box 600164, Hans-Knöll-Str. 10, 07745 Jena, Germany

Correspondence: Fortunat Joos (fortunat.joos@unibe.ch)

Received: 1 July 2024 – Discussion started: 26 July 2024
Revised: 4 November 2024 – Accepted: 7 November 2024 – Published: 3 January 2025

Abstract. Measurements of the seasonal cycle of $\delta^{13}C$ of atmospheric CO_2 ($\delta^{13}C_a$) provide information on the global carbon cycle and the regulation of carbon and water fluxes by leaf stomatal openings on ecosystem and decadal scales. Land biosphere carbon exchange is the primary driver of $\delta^{13}C_a$ seasonality in the Northern Hemisphere (NH). We use isotope-enabled simulations of the Bern3D-LPX (Land surface Processes and eXchanges) Earth system model of intermediate complexity and fossil fuel emission estimates with a model of atmospheric transport to simulate atmospheric $\delta^{13}C_a$ at globally distributed monitoring sites. Unlike the observed growth of the seasonal amplitude of CO_2 at northern sites, no significant temporal trend in the seasonal amplitude of $\delta^{13}C_a$ was detected at most sites, consistent with the insignificant model trends. Comparing the preindustrial (1700) and modern (1982–2012) periods, the modeled small-amplitude changes at northern sites are linked to the near-equal increase in background atmospheric CO_2 and the seasonal signal of the net atmosphere–land $\delta^{13}C$ flux in the northern extratropical region, with no long-term temporal changes in the isotopic fractionation in these ecosystems dominated by C_3 plants. The good data–model agreement in the seasonal amplitude of $\delta^{13}C_a$ and in its decadal trend provides implicit support for the regulation of stomatal conductance by C_3 plants towards intrinsic water use efficiency growing proportionally to atmospheric CO_2 over recent decades. Disequilibrium fluxes contribute little to the seasonal amplitude of the net land isotope flux north of 40° N but contribute near equally to the isotopic flux associated with growing season net carbon uptake in tropical and Southern Hemisphere (SH) ecosystems, pointing to the importance of monitoring $\delta^{13}C_a$ over these ecosystems. We propose applying seasonally resolved $\delta^{13}C_a$ observations as an additional constraint for land biosphere models and underlying processes for improved projections of the anthropogenic carbon sink.

1 Introduction

The seasonal variations in the carbon exchange fluxes between the atmosphere and the surface cause a seasonal cycle in atmospheric CO_2 (C_a) (Keeling et al., 1996; Graven et al., 2013; Masarie et al., 2014) and its stable isotopic signature ($\delta^{13}C_a$) (Keeling, 1960; Keeling et al., 1984, 1989, 2005; GLOBALVIEW-CO2C13, 2009), with $\delta^{13}C$ defined as $\delta^{13}C = [R_{sample}/R_{std} - 1] \times 1000$, where R_{sample} and R_{std} are the $^{13}C/^{12}C$ abundance ratios of the sample and the carbonate standard Pee Dee Belemnite (PDB; 0.0112372), respectively (Craig, 1957). Observations of the atmospheric seasonal cycles in background tropospheric air provide large-scale information on the carbon fluxes between the atmosphere, ocean, and land (Heimann et al., 1989, 1998) and constraints for models used to project C_a and global warming.

The additional information of $\delta^{13}C$ data in comparison to carbon data stems from differences in fractionation for different carbon fluxes. Carbon isotopic fractionation describes the preferential transfer of light ^{12}C compared to heavier ^{13}C. The degree of fractionation is different for the different physical, chemical, and biological processes (Mook, 1986), causing differences in the isotopic composition of carbon reser-

voirs and fluxes. The seasonal $\delta^{13}C_a$ variations result from the combination of carbon and isotopic fluxes from fossil fuel burning, land use, and the exchange of the atmosphere with the ocean and land biosphere. Comparing results of carbon-isotope-enabled models with observations of $\delta^{13}C_a$ is useful to assess whether the mix of carbon and isotopic sink and source fluxes is represented consistently in comparison with the observations. $\delta^{13}C_a$ observations offer, therefore, a benchmark for evaluating and improving Earth system models.

Fractionation is particularly large during the assimilation of CO_2 from the atmosphere by plants following the C_3 photosynthesis pathway, which are responsible for most of the global productivity (Still et al., 2003). Importantly, changes in isotopic fractionation by C_3 plants are indicative of changes in stomatal conductance, regulating the leaf-internal CO_2 mole fraction and thus photosynthesis (Farquhar, 1989; Saurer and Voelker, 2022; Cernusak and Ubierna, 2022). Photosynthesis, the associated water loss, and evaporative cooling are key characteristics of ecosystem function that are central to the cycles of carbon, nitrogen, water, and energy (Keenan et al., 2013; Knauer et al., 2017) and to the land sink of anthropogenic carbon. Acquisition of CO_2 for photosynthesis is accompanied by the loss of water through the stomatal pores that govern, by their conductance, the diffusion of these two gases between the leaf interior and the atmosphere. A key question is how ecosystems adjust their overall conductance and, thereby, co-regulate carbon uptake and plant growth, regulating water loss and evaporative cooling under rising C_a, growing nitrogen inputs to ecosystems, and increasing water vapor deficits under global warming. Many studies relying on multi-decadal- to century-scale tree-ring $\delta^{13}C$ records and free-air CO_2 enrichment (FACE) experiments suggest that small changes in isotopic fractionation and intrinsic water use efficiency, the ratio of assimilation to conductance, grow roughly proportionally with C_a (Voelker et al., 2016; Saurer et al., 2014; Kauwe et al., 2013; Peñuelas et al., 2011; Keller et al., 2017; Frank et al., 2015). In contrast, Battipaglia et al. (2013) and Keenan et al. (2013) suggest a scenario where conductance and the flows of carbon and water are downregulated under increasing C_a. Keeling et al. (2017), analyzing decadal-scale change in seasonally detrended $\delta^{13}C_a$ and the annual atmospheric budgets of carbon and ^{13}C, find a decrease in isotopic fractionation of global mean net primary production; the change is attributed to changes in fractionation associated with mesophyll conductance and photorespiration of C_3 plants, and intrinsic water use efficiency is inferred to grow proportionally with C_a. Conflicting results for 20th-century changes in fractionation and intrinsic water use efficiency are also found in global land biosphere models (Keller et al., 2017).

The observational records from globally distributed monitoring sites (Keeling et al., 1996; Graven et al., 2013; Masarie et al., 2014) demonstrate a significant growth trend in the seasonal cycle amplitude (SA) of C_a (Bacastow et al., 1985; Keeling et al., 1996; Graven et al., 2013; Barlow et al., 2015; Piao et al., 2018) driven by changes in the seasonality of net land carbon uptake (Graven et al., 2013; Forkel et al., 2016). The observed seasonal cycle and amplitude growth of C_a are widely used to evaluate carbon cycle models and system understanding by transporting fluxes from terrestrial, oceanic, and fossil fuel sources with a model of atmospheric transport to obtain local C_a anomalies (Heimann et al., 1998; Dargaville et al., 2002; Scholze et al., 2008; Peng et al., 2015; Lienert and Joos, 2018). Studies address the role of different climatic drivers and terrestrial carbon cycle processes such as drought, land use, warming, productivity, and soil respiration (Heimann et al., 1989, 1998; Graven et al., 2013; Forkel et al., 2016; Ito et al., 2016; Bastos et al., 2019; Wang et al., 2020) and surface-to-atmosphere C fluxes (e.g., Peylin et al., 2013). SAs(C_a) and their temporal trends at different monitoring sites are used for constraining an ensemble of land biosphere model simulations (Lienert and Joos, 2018).

Comparable studies analyzing the temporal trends in SA($\delta^{13}C_a$) and the seasonal cycle of $\delta^{13}C_a$ are scarce. While seasonally resolved atmospheric $\delta^{13}C_a$ measurements are available (GLOBALVIEW-CO2C13, 2009; Keeling et al., 2001), these seasonally resolved records are yet to be fully utilized in the context of process-based carbon cycle models. Heimann et al. (1989) simulated the spatiotemporal distribution of $\delta^{13}C_a$ and C_a with an atmospheric transport model using estimates of net primary production (NPP) and heterotrophic respiration based on satellite data and surface temperature and prescribed surface ocean CO_2, demonstrating the dominant role of land biosphere fluxes for Northern Hemisphere (NH) seasonality and finding relevant signals from the ocean and land in the Southern Hemisphere (SH). Van der Velde et al. (2018) applied their CarbonTracker Data Assimilation System for CO_2 and $^{13}CO_2$ by varying the net exchange fluxes of CO_2 and $^{13}CO_2$ in ocean and terrestrial biosphere models and propagating the fluxes through an atmospheric transport model to solve for weekly adjustments to fluxes and isotopic terrestrial discrimination, minimizing differences between observed and estimated mole fractions. They identified a decrease in stomatal conductance on a continent-wide scale during a severe drought. Ballantyne et al. (2011) applied an analytical regression approach to analyze the differences in isotopic signatures between Northern Hemisphere site data and free-troposphere background data from Niwot Ridge to infer seasonal variations in the source signature of the net atmosphere–land biosphere flux and to evaluate models of stomatal conductance. Observations of $\delta^{13}C_a$ seasonal cycles were used to investigate isotopic fractionation (Ballantyne et al., 2010) and trends in the phenology of northern terrestrial ecosystems (Gonsamo et al., 2017) but to our knowledge have not been used for analyzing trends in SA($\delta^{13}C_a$) globally.

This study addresses the following main questions:

1. Is the seasonal cycle of $\delta^{13}C_a$ observed at a network of globally distributed sites represented well in model simulations? How large are the contributions of ocean, land, and fossil fuel fluxes to $\delta^{13}C_a$ seasonality?

2. What are the temporal trends in SA($\delta^{13}C_a$) in the observational records, and are the modeled trends in SA($\delta^{13}C_a$) consistent with the observed trends?

3. What are the different drivers of SA($\delta^{13}C_a$) versus SA(C_a) and of their temporal trends? Is a model scenario with intrinsic water use efficiency growing proportional with C_a consistent with $\delta^{13}C_a$ seasonality data?

We simulate atmospheric $\delta^{13}C_a$ and C_a at 19 globally distributed sites using the matrix representation of an atmospheric transport model and net atmosphere-to-surface fluxes of CO_2 and $\delta^{13}(CO_2)$ from an Earth system model of intermediate complexity (EMIC) alongside gridded fossil fuel emission estimates and changes in land use and the distribution of C_3 and C_4 crops. We compare model results to observations and analyze trends in SA($\delta^{13}C_a$) using the records of the Scripps CO_2 program (Keeling et al., 2001) and the Cooperative Global Atmospheric Data Integration Project (2013) product. We discuss the implications of our results for changes in the fractionation by C_3 plants, their stomatal controls, and associated carbon and water fluxes. We develop a theoretical framework to explain the trends in SA($\delta^{13}C_a$) and decompose net carbon and isotope land biosphere fluxes into underlying component fluxes and changes in carbon fluxes and fractionation. The framework could serve future studies, e.g., studies applying an ensemble of different models for multi-model evaluation, and provide more robust conclusions in comparison to using a single model chain.

2 Methods

2.1 Bern3D-LPX Earth system model of intermediate complexity

Spatially resolved surface-to-atmosphere CO_2 and $^{13}CO_2$ fluxes are simulated with the Bern3D-LPX (Land surface Processes and eXchanges) Earth system model of intermediate complexity. Here, the ocean–atmosphere model Bern3D (Jeltsch-Thömmes and Joos, 2020; Battaglia and Joos, 2018; Ritz et al., 2011) is coupled to the dynamic global vegetation model (DGVM) framework of the Land surface Processes and eXchanges (LPX) model, LPX-Bern v1.4 (Lienert and Joos, 2018). The Bern3D model features a 41×40 horizontal ocean grid (about $9° \times 4.5°$) with 32 depth layers coupled to a single-layer energy–moisture balance atmosphere (Ritz et al., 2011). In Bern3D, carbon and its isotopes are implemented as tracers with fractionation for air–sea and sea–air gas exchange, aquatic chemistry, and the production of organic material and $CaCO_3$ as a function of surface ocean temperature, aqueous CO_2, and the speciation of dissolved inorganic carbon, as described by Jeltsch-Thömmes and Joos (2023). LPX-Bern simulates the coupled cycling of carbon, nitrogen, and water (Xu-Ri and Prentice, 2008; Wania et al., 2009a, b; Stocker et al., 2014) and vegetation dynamics using plant functional types (Sitch et al., 2003). It is run here at a $3.75° \times 2.5°$ resolution. Grid cells are subdivided into different land use classes (mineral soil, wetlands, crop, pasture, urban). Carbon isotopes were added (Scholze et al., 2003) using a photosynthetic fractionation scheme (Lloyd and Farquhar, 1994) and without further isotopic fractionation during the transfer through the vegetation, litter, soil, and product pools. The scheme neglects fractionation by boundary layer transport and ternary effects associated with the interaction of CO_2, water, and air (Farquhar and Cernusak, 2012), and fractionation by dark-day respiration is set to zero, while fractionation by the following terms is explicitly considered: stomatal conductance (with a scaling factor of 4.4 ‰), dissolution and liquid transport (1.8 ‰), carboxylation (27.5 ‰), and photorespiration (8 ‰ and the CO_2 compensation point that would occur in the absence of dark respiration, Γ^*, increases with temperature) (Lloyd and Farquhar, 1994). The signature of respired carbon reflects the signature of carbon assimilated at previous times; the lag times between assimilation and respiration are dictated by the turnover timescales of the various pools, depending on temperature and soil moisture. Land carbon and isotope fluxes respond to altered climate, which influences, for example, photosynthesis through temperature and water limitation, fire frequency, and autotrophic and heterotrophic respiration rates; respond to increasing C_a, which stimulates photosynthesis and affects water use efficiency ("CO_2 fertilization"); respond to land use (Strassmann et al., 2008), which causes, for example, transfer of tree carbon to the atmosphere, litter, and product pools after deforestation and shifts from natural vegetation to C_3 and C_4 crops and pasture; and respond to altered nitrogen deposition and the addition of nitrogen fertilizer on managed land alleviating nitrogen limitation.

Bern3D and LPX-Bern were spun up individually, followed by a 500-year coupled spinup to preindustrial equilibrium (1700 CE; 276.3 ppm, −6.27 ‰). A transient simulation, E_{standard}, from 1700 to 2020 is driven by annual fossil fuel carbon emissions (including the contribution from cement production) (Friedlingstein et al., 2020), net land use area changes (Hurtt et al., 2020), and non-CO_2 radiative forcing. $\delta^{13}C$ of the fossil fuel emissions follows Andres et al. (2017) for 1751–2014 and is set to the value for 1751 before. For 2014–2020, signatures of major source categories (coal, oil, gas, cement) are assumed to be constant and combined with the emission sources from Friedlingstein et al. (2020), following the approach of Andres et al. (2000). Here, we explicitly distinguish land use classes for C_3 and C_4 crops and prescribe their extent, and net land use area changes are based on the Land-Use Harmonization 2 dataset (Hurtt et al., 2020). Nitrogen deposition and nitrogen fertilization are taken from the Global N_2O Model Intercomparison Project (Tian et al.,

2018). Nitrogen (N) is a limiting nutrient in LPX, and plant growth is downregulated under N stress, which tends to reduce plant growth and plant growth responses to rising C_a compared to a model with absent N cycling. The monthly wind stress climatology from the NCEP/NCAR Reanalysis produced by the National Centers for Environmental Prediction (NCEP) and the National Center for Atmospheric Research (NCAR) (Kalnay et al., 1996) is prescribed to the ocean. Climatic Research Unit (CRU) Time Series (TS) version 4.05 high-resolution gridded data of month-by-month variation in climate (CRU TS v4.05) (Harris et al., 2020) are used for the land model. For 1700–1900 and the spinup, the climate of 1901–1931 is recycled. A baseline is provided by a control simulation, termed E_{control}, without anthropogenic CO_2 emissions; absent radiative forcing from non-CO_2 species (e.g., from CH_4, N_2O, ozone); and with land use, nitrogen deposition, and nitrogen fertilization at the 1700 level, as well as recycling the 1901–1931 land climate. C_a and $\delta^{13}C_a$ evolve freely in all simulations presented and remain at their preindustrial values in E_{control}.

2.2 Atmospheric transport model TM3 and the seasonal cycles of C_a and $\delta^{13}C_a$

We employ the transport matrices of the global atmospheric tracer model TM3, a three-dimensional transport model (Heimann and Körner, 2003; Kaminski et al., 1998; Schürmann et al., 2016), to translate surface–atmosphere fluxes from Bern3D-LPX and fossil fuel emissions into C_a and $\delta^{13}C_a$ anomalies at 19 measurement sites across the globe. Before transport, the fluxes are remapped to the TM3 grid with 72×48 grid cells ($5° \times 3.75°$). Here, the matrices span 1982 to 2012 and are only available if there is also a CO_2 measurement available at the corresponding site. Each matrix represents the sensitivity of the local atmospheric concentration for a given month to the local surface fluxes of the previous period, spanning up to 48 months. The transport model is initialized with equal C_a and $\delta^{13}C_a$ at all sites.

For ^{13}C, the signature-weighted net atmosphere-to-surface flux is

$$\delta^{13} f_{\text{as,net}}(\boldsymbol{x}, t) = f_{\text{as,net}}(\boldsymbol{x}, t) \cdot \delta^{13}C_{\text{as,net}}(\boldsymbol{x}, t). \quad (1)$$

$\delta^{13} f_{\text{as,net}}$ is in units of mol ‰ m^{-2} yr^{-1}. $\boldsymbol{x}$ indicates location and t time at the monthly and spatial ($5° \times 3.75°$) resolution of TM3. The net carbon fluxes ($f_{\text{as,net}}$; mol m^{-2} yr^{-1}); their signatures ($\delta^{13}C_{\text{as,net}}$); and, therefore, $\delta^{13} f_{\text{as,net}}$, are readily available for fossil fuel emissions, including cement production (Andres et al., 2009a, b). Bern3D-LPX simulates two-way exchange of CO_2 and $^{13}CO_2$ from and to the ocean and land surface. Net transfer rates are determined by the difference in these gross fluxes to yield the atmosphere-to-surface net fluxes, $f_{\text{as,net}}$ and $\delta^{13} f_{\text{as,net}}$, of Bern3D-LPX.

The matrices are applied with $f_{\text{as,net}}$ to compute anomalies in C_a and with $\delta^{13} f_{\text{as,net}}$ to compute anomalies in $^{13}CO_2$. We get $\delta^{13}C_a$ from $^{13}CO_2/C_a$. This method of transporting signature-weighted net fluxes was chosen instead of separately transporting $^{13}CO_2$ and $^{12}CO_2$. Both approaches were tested and showed very similar results, except for numerical issues in months having very small local $^{12}CO_2$ anomalies for the second approach.

Ocean, land, and fossil fuel fluxes from the standard simulation are transported separately to quantify the contributions of these individual components to the seasonal variations in C_a and $\delta^{13}C_a$. For E_{control}, fossil fuel fluxes are not transported, consistent with the model setup. A limitation is that transport matrices are only available for the period of 1982 to 2012, limiting the analysis period and direct model–data comparison to 3 decades only.

2.3 Site data

Background CO_2 from 19 monitoring sites for which transport matrices are available is used for comparison with simulated C_a and $\delta^{13}C_a$ and to determine observation-based trends in their SAs. The Cooperative Global Atmospheric Data Integration Project (2013) product is used for C_a. For $\delta^{13}C_a$, the records of the Scripps CO_2 program (Keeling et al., 2001) for Alert, Mauna Loa, and the South Pole from monthly averaged flask data are used. These records span a longer period than the available transport matrices. For the remaining 16 sites, the shorter (1994 to 2009) records of GLOBALVIEW-CO2C13 (2009) are used. In the main paper, we focus on 3 out of the 19 available transport sites: Alert (82.5° N, Canada), Mauna Loa (19.5° N, Hawaii), and the South Pole (90° S, Antarctica). Results for the other sites are shown in the Supplement and Table 1. The Scripps and GLOBALVIEW-CO2C13 data are on slightly different scales (Lueker et al., 2020); this does not affect our analysis of seasonal anomalies. The $\delta^{13}C_a$ records of GLOBALVIEW-CO2C13 (2009) span the order of a decade and are, therefore, not used for trend detection, although we evaluated trends from the simulations for the GLOBALVIEW sites (Table 2, excluding Key Biscayne). We require at least 10 monthly values for a year to be included in the linear regression.

Additional $\delta^{13}C_a$ monthly flask data from the Scripps CO_2 program (Keeling et al., 2001) are used for analyzing temporal trends in the SA($\delta^{13}C_a$). We focus on eight sites with more than 20 years of data: Alert (ALT, 82° N), Nuvuk (formerly Point Barrow) (PTB, 71° N), La Jolla (LJO, 33° N), Mauna Loa Observatory (MLO, 20° N), Cape Kumukahi (KUM, 20° N), Christmas Island (CHR, 2° N), Samoa (SAM, 14° S), and the South Pole (SPO, 90° S). The data are provided as (i) monthly samples, (ii) a fit to these monthly samples, and (iii) the monthly samples but with missing values replaced by fitted values. We also used the original, non-gap-filled data and years with at least 9, 10, or 11 monthly values per year in the regression.

3 The influence of carbon and isotope fluxes on the seasonal cycles of C_a and $\delta^{13}C_a$: a conceptual framework

We develop a simplified conceptual framework to qualitatively explore the influence of carbon and isotope fluxes on the seasonal cycles of C_a and $\delta^{13}C_a$. For illustration, the atmosphere is considered to be well-mixed in this section; the atmospheric transport operator is linear, and the findings may qualitatively also apply to spatially resolved fluxes. The budgets for the atmospheric inventories of carbon and ^{13}C are approximated (Tans et al., 1993) as

$$\frac{\mathrm{d}}{\mathrm{d}t}N_a = -F_{as,net} \tag{2}$$

$$\frac{\mathrm{d}}{\mathrm{d}t}(N_a \cdot \delta^{13}C_a) = \left(\frac{\mathrm{d}}{\mathrm{d}t}N_a\right)\cdot\delta^{13}C_a + N_a\cdot\left(\frac{\mathrm{d}}{\mathrm{d}t}\delta^{13}C_a\right) = -F_{as,net}\cdot\overline{\delta^{13}C_{as,net}}. \tag{3}$$

N_a and $N_a\cdot\delta^{13}C_a$ are the atmospheric inventories of carbon and (approximately) of ^{13}C (in mol‰). $F_{as,net}$ and $F_{as,net}\cdot\overline{\delta^{13}C_{as,net}}$ are the globally integrated net atmosphere-to-surface carbon and ^{13}C flux; $\overline{\delta^{13}C_{as,net}}$ is the signature of the global net carbon flux. We set $N_a = c\cdot C_a$, where c is a unit conversion factor. Solving Eqs. (2) and (3) for the changes in C_a and $\delta^{13}C_a$ yields

$$\frac{\mathrm{d}}{\mathrm{d}t}C_a = \frac{-1}{c}\cdot F_{as,net} \tag{4}$$

$$\frac{\mathrm{d}}{\mathrm{d}t}\delta^{13}C_a = \frac{-1}{c\cdot C_a}\cdot\delta^{13}F^*_{as,net}, \tag{5}$$

with $\delta^{13}F^*_{as,net}$ being the global integral of

$$\delta^{13}f^*_{as,net} = f_{as,net}\cdot\left(\delta^{13}C_{as,net} - \delta^{13}C_a\right). \tag{6}$$

The superscript * indicates that the ^{13}C fluxes (e.g., in units of mol‰ yr^{-1} m^{-2} for $\delta^{13}f^*_{as,net}$) are referenced to the atmospheric signature. Equation (6) corresponds to Eq. (1) for the net atmosphere-to-surface isotopic flux but is now referenced to the atmospheric signature instead of the signature of 0‰ of the Vienna Pee Dee Belemnite standard as in Eq. (1). In this way, a positive (negative) flux causes a negative (positive) change in $\delta^{13}C_a$.

Equations (4) and (5) are readily integrated over the growing season from the intra-annual maximum to the minimum (subscripts indicate max and min) in C_a and the corresponding beginning, t_{beg}, and end, t_{end}, of the growing season to get the seasonal cycle amplitude (SA) for the two tracers and (cumulative) net fluxes (see Appendix A for calculation of SA for a flux):

$$\underbrace{C_{a,max} - C_{a,min}}_{SA(C_a)} = \underbrace{\frac{1}{c}\int_{t_{beg}}^{t_{end}} F_{as,net}(t)\,\mathrm{d}t}_{SA(F_{as,net})} \tag{7}$$

$$\underbrace{\delta^{13}C_{a,max} - \delta^{13}C_{a,min}}_{SA(\delta^{13}C_a)} = \underbrace{\frac{-1}{c\cdot C_a}\int_{t_{beg}}^{t_{end}} \delta^{13}F^*_{as,net}(t)\,\mathrm{d}t}_{SA(\delta^{13}F^*_{as,net})}. \tag{8}$$

Equations (5) and (8) provide important insights. First, changes in $\delta^{13}C_a$ and its seasonal cycle are driven by $\delta^{13}F^*_{as,net}$; seasonal changes in C_a, the denominator in Eq. (5), are small compared to C_a, and C_a is considered constant within a given year (the error associated with this approximation is less than 3 %). Second, the background CO_2 mole fraction, C_a, modulates the magnitude of the $\delta^{13}C_a$ seasonal cycle. $SA(\delta^{13}C_a)$ would be larger under low preindustrial C_a than under modern C_a for equal seasonal variations in $\delta^{13}F^*_{as,net}$. Correspondingly, $SA(\delta^{13}C_a)$ does not change over time as long as the relative changes in $SA(\delta^{13}F^*_{as,net})$ and in C_a are equal. Equations (7) and (8) were derived for a globally well-mixed atmosphere and global fluxes but analogously also apply for the tracer seasonality at individual sites, with the integral on the right-hand side of Eqs. (7) and (8) representing the integral of (transport-weighted) fluxes over the region influencing tracer seasonality at the site. We recall that the above equations and conclusions were derived by assuming a well-mixed atmosphere, while in reality spatial flux patterns and transport and their changes influence seasonal cycles at individual atmospheric sites. Further, the start and end of the growing season are assumed to coincide with the switch in the sign of the isotopic flux; this is the case in our model for zonally integrated fluxes. These seasonal fluxes will be presented in Sect. 4.3. Equations (2) to (8) are for illustrating the influence of carbon and carbon isotope fluxes on the seasonal cycles of C_a and $\delta^{13}C_a$; they were not used for calculating numerical results.

The notation and sign convention introduced above are applied in this paper. In brief, $f_{i,j}$ defines a one-way flux from the source reservoir i to the receiving reservoir j and is positive. The isotopic signature of this flux is $\delta^{13}C_{i,j}$. The net flux from reservoir i to reservoir j is $f_{i,j,net}$ and is the difference between the corresponding one-way fluxes; e.g., $f_{i,j,net} = f_{i,j} - f_{j,i}$. $f_{i,j,net}$ is positive if the net flux results in the transfer of mass from i to j.

4 Results

4.1 Seasonal cycles of atmosphere–surface fluxes, C_a, and $\delta^{13}C_a$

The Bern3D-LPX model simulates ($E_{standard}$) large seasonal variations in the net land biosphere–atmosphere exchange of CO_2 and $^{13}CO_2$, whereas seasonal variations in ocean–atmosphere fluxes are much smaller (Fig. 1). This seasonality is broadly consistent with estimates of regional air–land carbon flux seasonality from an atmospheric inversion (Gurney et al., 2004) and air–sea flux seasonality from surface

Table 1. The seasonal cycle amplitude of C_a and $\delta^{13}C_a$ from the standard simulation (mod; $E_{standard}$) and observations (obs) for 19 monitoring sites and the period of 1982–2012. The increase over the industrial period is estimated from the difference between the standard simulation and the preindustrial control ($100 \cdot (E_{standard} - E_{control})/E_{control}$).

Site	Seasonal cycle amplitude of C_a				Seasonal cycle amplitude of $\delta^{13}C_a$			
	Model [ppm]	Observed [ppm]	Mod–obs [ppm]	Increase [%]	Model [‰]	Observed [‰]	Mod–obs [‰]	Increase [%]
Alert, Nunavut, Canada (82° N)	17.26 ± 0.84	14.82 ± 0.75	2.44	41	0.719 ± 0.035	0.750 ± 0.042	−0.030	8
Nuvuk (formerly Point Barrow), Alaska, US (71° N)	20.10 ± 1.06	15.79 ± 0.75	4.31	37	0.899 ± 0.041	0.822 ± 0.030	0.077	6
Ocean Station M, Norw. (66° N)	17.73 ± 1.14	14.77 ± 0.93	2.96	36	0.763 ± 0.051	0.752 ± 0.028	0.010	4
Cold Bay, Alaska, US (55° N)	14.83 ± 0.80	15.91 ± 1.00	−1.08	39	0.657 ± 0.032	0.847 ± 0.029	−0.190	4
Shemya Island, Alaska, US (53° N)	14.63 ± 0.88	17.03 ± 0.98	−2.40	37	0.655 ± 0.038	0.926 ± 0.029	−0.271	3
Mace Head, Ireland (53° N)	14.65 ± 1.15	13.64 ± 1.74	1.01	42	0.618 ± 0.046	0.726 ± 0.039	−0.107	6
Terceira Island, Portugal (39° N)	11.70 ± 0.86	9.39 ± 1.18	2.31	36	0.497 ± 0.028	0.517 ± 0.036	−0.020	−1
Key Biscayne, Florida, US (26° N)	8.97 ± 0.78	8.17 ± 2.31	0.79	33	0.350 ± 0.031	0.405 ± 0.040	−0.055	−6
Mauna Loa, Hawaii, US (20° N)	8.33 ± 0.30	6.51 ± 0.24	1.82	38	0.328 ± 0.013	0.339 ± 0.028	−0.010	4
Cape Kumukahi, Hawaii, US (20° N)	9.07 ± 0.39	7.96 ± 0.53	1.11	41	0.358 ± 0.017	0.423 ± 0.028	−0.065	5
Mariana Islands, Guam (13° N)	6.36 ± 0.41	6.11 ± 0.72	0.26	39	0.254 ± 0.019	0.312 ± 0.022	−0.058	3
Ragged Point, Barbados (13° N)	8.00 ± 0.39	7.10 ± 0.45	0.89	38	0.306 ± 0.017	0.332 ± 0.027	−0.026	9
Christmas Island, Kiribati (2° N)	4.68 ± 0.35	2.95 ± 0.38	1.74	77	0.161 ± 0.016	0.129 ± 0.018	0.033	52
Mahe Island, Seychelles (5° S)	3.52 ± 0.41	2.57 ± 0.53	0.95	175	0.145 ± 0.015	0.113 ± 0.021	0.032	63
Ascension Island, UK (8° S)	3.17 ± 0.41	1.81 ± 0.44	1.37	8	0.134 ± 0.012	0.073 ± 0.016	0.061	−28
Tutuila, American Samoa (14° S)	1.29 ± 0.28	0.89 ± 0.30	0.40	51	0.044 ± 0.007	0.020 ± 0.009	0.024	−8
Palmer Station, Antarctica (65° S)	2.60 ± 0.25	1.41 ± 0.19	1.20	21	0.107 ± 0.008	0.037 ± 0.008	0.070	−17
Halley Station, Antarctica (76° S)	2.57 ± 0.15	1.09 ± 0.16	1.48	32	0.103 ± 0.005	0.027 ± 0.007	0.076	−5
South Pole, Antarctica (90° S)	2.06 ± 0.16	1.09 ± 0.11	0.97	20	0.094 ± 0.004	0.033 ± 0.015	0.061	−4

ocean pCO_2 observations (Landschützer et al., 2014; Takahashi et al., 2009; Fay et al., 2021), except in the Southern Ocean and in the northern subpolar gyres. The LPX land biosphere model shows the expected uptake of isotopically depleted carbon, resulting in positive $f_{as,net}$ and negative $\delta^{13} f^*_{as,net}$ during the summer and vice versa in winter.

The Bern3D ocean model shows a negative $\delta^{13} f^*_{as,net}$ in the low latitudes and midlatitudes, small modern fluxes in the northern subpolar gyres, and a positive flux in the Southern Ocean in both seasons (Fig. 1). These modern Bern3D fluxes are driven by the atmosphere–ocean isotopic disequilibrium, here defined as the isotopic signature of the atmosphere-to-surface carbon flux minus the signature of the surface-to-atmosphere flux ($\delta_{dis,as}$; Eq. A2), with a negative $\delta_{dis,as}$ in the low latitudes and midlatitudes, a small modern disequilibrium in northern high latitudes, and a positive $\delta_{dis,as}$ south of 50° S, consistent with observations (Menviel et al., 2015; Quay et al., 2017; Becker et al., 2018).

The preindustrial $\delta_{dis,as}$ and $\delta^{13} f^*_{as,net}$ are negative in the low latitudes and midlatitudes and positive in high-latitude ocean regions (not shown), mainly driven by the temperature dependency of isotopic fractionation during air–sea exchange and the cycling of marine biological matter (see Fig. 1 of Menviel et al., 2015, to compare Bern3D and LOVECLIM results for $\delta_{dis,as}$). Fossil fuel emissions cause a negative flux perturbation worldwide, shifting the net isotopic fluxes to more negative values over the industrial period.

Figure 2 compares the mean seasonal cycles of C_a and $\delta^{13}C_a$ from $E_{standard}$ with measurements from 1982 (at Alert from 1985) to 2012 at three sites and with factorial simulations, where the fluxes of the land (dashed green line), ocean (dashed blue line), and fossil fuel emissions (dashed brown lines) were considered individually (see Table 1 and Figs. S1 and S2 in the Supplement for additional sites). For the Northern Hemisphere (NH) sites of Alert (top panels) and Mauna Loa (middle panels), the seasonal variations are dominated by the terrestrial biosphere fluxes, with minor contributions from ocean fluxes and fossil fuel emissions.

Both the timing and amplitude of the observed seasonal cycle of C_a and $\delta^{13}C_a$ are captured reasonably well by $E_{standard}$ (Fig. 2). The simulated SA(C_a) and its interannual variability (IAV) are overestimated compared to observations at Alert (17.3 ± 0.84 ppm versus 14.8 ± 0.75 ppm) and Mauna Loa (8.3 ± 0.30 ppm versus 6.5 ± 0.24 ppm). SA($\delta^{13}C_a$) matches the observations (ALT – 0.72 ± 0.035 ‰ versus 0.75 ± 0.042 ‰; MLO – 0.34 ± 0.013 ‰ versus 0.33 ± 0.028 ‰). Good model–data agreement in the phasing of the seasonal cycle of C_a relative to $\delta^{13}C_a$ is demonstrated for Alert in panel (c), where monthly anomalies in $\delta^{13}C_a$ are plotted versus anomalies in C_a. Both the observations and the model show hysteresis throughout the year, with the loop rotating clockwise. At Mauna Loa, the rotation direction of the hysteresis loop is clockwise in the simulation and counterclockwise in the observations (panel f). Still, the observed hysteresis is small, with offsets of less than 0.03 ‰. The hysteresis arises as the ratio between the rate of change in $\delta^{13}C_a$ versus the rate of change in C_a varies over the year (Keeling et al., 1989; Heimann et al., 1989). This non-linearity in the atmospheric tracer relationship originates from seasonally varying transport in combination with spatially and temporally varying relationships of atmosphere–surface $\delta^{13}C$ to

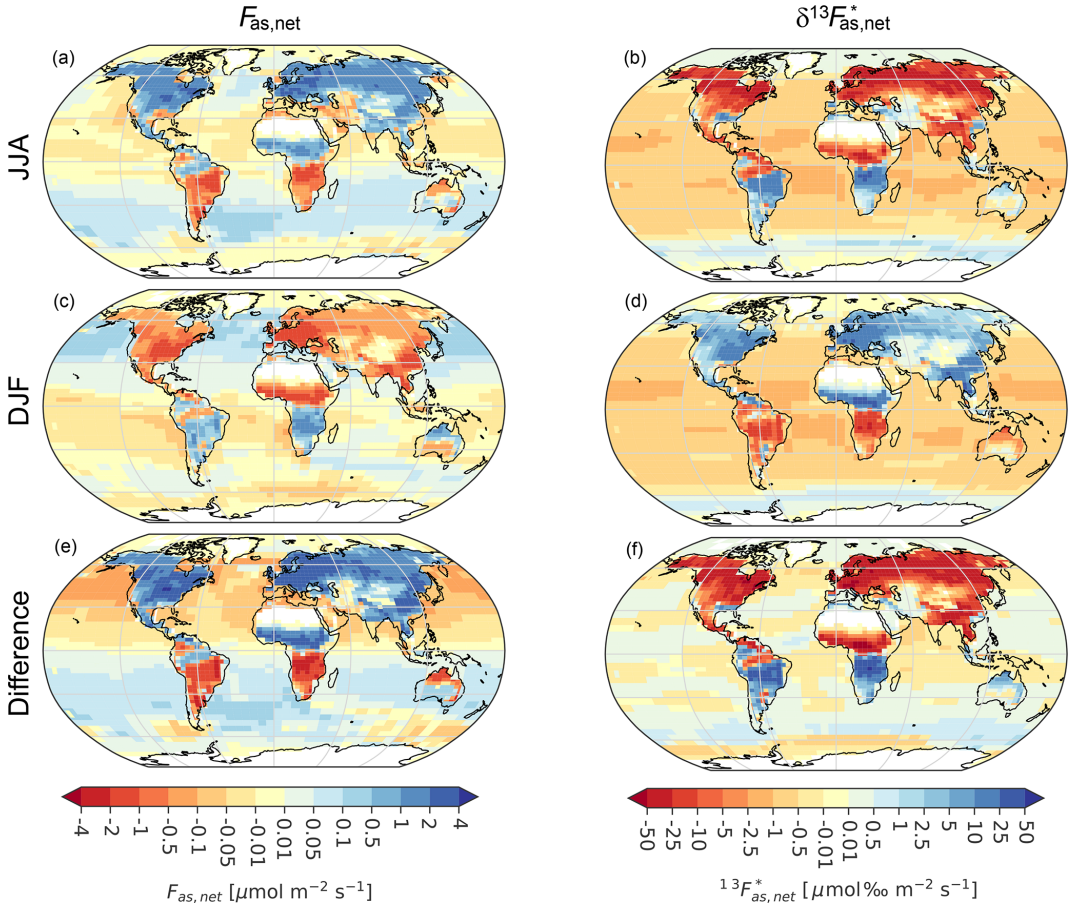

Figure 1. Net seasonal atmosphere-to-surface fluxes. Fluxes are for **(a, c, e)** carbon and **(b, d, f)** the δ^{13}C-weighted carbon flux, $\delta^{13} f^{*}_{\mathrm{as,net}}$ (see Sect. 3), from the standard simulation (E_{standard}) and are averaged over 1982–2012 for **(a, b)** June, July, and August (JJA); **(c, d)** December, January, and February (DJF); and **(e, f)** JJA minus DJF. Note the non-linear color bars with blue colors in panels **(a)** to **(d)** indicating a lowering in atmospheric CO_2 and δ^{13}C.

CO_2 flux. For example, the isotopic signature of the growing season net atmosphere-to-land carbon flux $\delta^{13}C_{\mathrm{al,net}}$ is -13.4 ‰ for the northern high-latitude region (>40° N) but only -10.7 ‰ for the region 10–40° N, and the signal observed at any measurement site results from varying contributions from these and other latitudinal bounds given intra-annually varying winds and hence transport.

Results for the South Pole are different than for the NH sites (Fig. 2g, h, i). Neither the timing nor the amplitude of C_a (2.1 ± 0.16 ppm simulated versus 1.1 ± 0.11 ppm observed) and $\delta^{13}C_a$ (0.094 ± 0.004 ‰ versus 0.033 ± 0.015 ‰) agrees with observations. SA(C_a) and SA($\delta^{13}C_a$) at the South Pole are observed to be 14 and 23 times smaller than at Alert, respectively. The absolute data–model mismatches are therefore not as drastic as the relative mismatches. The disagreement between simulation and observational estimates is also apparent when considering the scatter plot in panel (i). The model shows a complex hysteresis relationship, whereas the observations display a clockwise loop.

The remote Antarctic sites (the South Pole, Palmer, and Halley) show an expected relatively larger dependence on the ocean, but the terrestrial contribution still dominates in the model (Figs. 2, S1, and S2). The C_a seasonal cycle resulting from atmosphere–ocean flux is shifted by up to 6 months compared to observations at the South Pole and the other two Antarctic sites (Palmer, Halley; blue lines versus black dots in Fig. S1), pointing to biases in the Bern3D ocean flux. Observation-based analyses indicate stronger ocean CO_2 uptake in summer than in winter in the Southern Ocean (Jin et al., 2024; Long et al., 2021; Fay et al., 2021) in contrast to results from Bern3D (Fig. 1) and more complex ocean models (Hauck and Völker, 2015) and several Earth system models from CMIP5 (Majkut et al., 2014) and CMIP6 (Joos et al., 2023). The simulated amplitude and phasing of the $\delta^{13}C_a$ seasonal cycle resulting from the ocean are broadly in line with observations at the Antarctic sites (Fig. S2). The air–sea isotopic disequilibrium is large in the Southern Ocean, and the two-way air–sea and sea–air exchange fluxes yield a substantial net isotopic flux, even under low net carbon

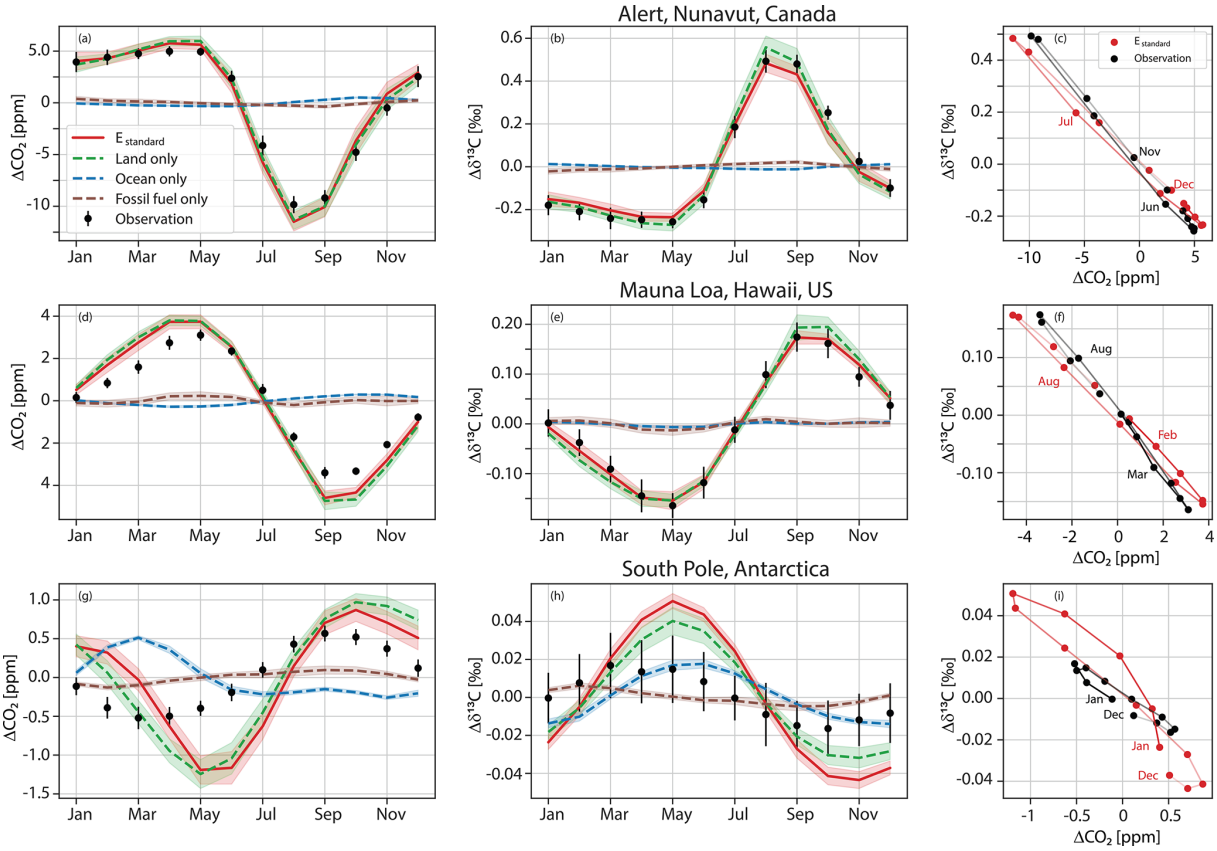

Figure 2. The simulated (red) seasonal cycle of atmospheric C_a (left, **a, d, g**) and its signature $\delta^{13}C_a$ (middle, **b, e, h**) compared to observations (black dots). In the rightmost panels **(c, f, i)** the seasonal anomalies (Δ) of C_a are plotted against those of $\delta^{13}C_a$, with lines connecting the monthly values (dots) fading from January to December. Results are for Alert, northern Canada **(a, b, c)**; Mauna Loa, Hawaii **(d, e, f)**; and the South Pole **(g, h, i)**. Simulated values are from transporting net TM3 fluxes of the Bern3D-LPX $E_{standard}$ simulation from all (red, $E_{standard}$), terrestrial (green, dashed), oceanic (blue, dashed), and fossil fuel sources (brown, dashed). The observational and model anomalies are computed from monthly values between 1982 and 2012 if both the measurements and transport matrices are available. Error bars and shading correspond to the standard deviation from the interannual variability in monthly values.

flux. Temperature-dependent fractionation is higher in winter than in summer, and the air–sea gas exchange piston velocity and, in turn, the isotope fluxes are larger under high winds in winter than in summer in the modeled Southern Ocean, consistent with the observed seasonal phasing of $\delta^{13}C_a$ at the Antarctic sites. Errors in modeled Southern Ocean fluxes are expected to have a minor impact on simulated $SA(C_a)$ and $SA(\delta^{13}C_a)$ at NH sites, where the influence of land fluxes dominates by far (Figs. 2, S1, S2).

Considering all extratropical Northern Hemisphere sites, model–data mismatches are less than 30 % for $SA(C_a)$ and $SA(\delta^{13}C_a)$ and their root-mean-square errors (RMSEs) are 2.6 ppm and 0.14 ‰, respectively. For the tropical and SH sites, large relative data–model deviations of up to 140 % for $SA(C_a)$ and up to 290 % for $SA(\delta^{13}C_a)$ are evident, although absolute deviations are less than 1.8 ppm, and 0.18 ‰ and the corresponding RMSEs are 1.2 ppm and 0.05 ‰ (Table 1).

Interannual variability in simulated $SA(\delta^{13}C_a)$ compares reasonably well with observations at sites in the NH subtropics and extratropics (average of the 1σ standard deviation of 12 sites is 0.031 ‰ in $E_{standard}$ versus 0.031 ‰ in observations) and in the tropics and SH (0.009 ‰ versus 0.013 ‰) (Table 1). Similar agreement between simulated and observation-derived IAV holds for $SA(C_a)$ (NH extratropics –0.75 versus 0.96 ppm; tropics and SH – 0.29 versus 0.30). This suggests that the variability in the seasonal amplitude of the carbon and isotope fluxes is reasonably represented by LPX-Bern. The correct simulation of variability can be challenging and van der Velde et al. (2013) report too low an interannual variability in the annually integrated isotopic disequilibrium flux for their model.

4.2 Temporal trends in the seasonal cycle amplitude of $\delta^{13}C_a$ and C_a

Detection of trends in $SA(\delta^{13}C_a)$ may be hampered by interannual-to-decadal variability, short record lengths, and a small $SA(\delta^{13}C_a)$ in comparison to measurement uncertainty

and variability, as is typical at Southern Hemisphere sites. For example, dividing SA($\delta^{13}C_a$) by 2 standard deviations of IAV yields a signal-to-noise ratio (Keller et al., 2014) below 2.7 at SH sites and as low as 1.1 at the South Pole and on American Samoa (Table 1). Thus, SA($\delta^{13}C_a$) would need to roughly double over the observational period for a trend in SA($\delta^{13}C_a$) to emerge from the noise of IAV at these two sites. The situation is more favorable for trend detection at NH extratropical sites (Table 1), where the signal-to-noise ratio ranges between 9 and 16, and changes of 6 % to 11 % in SA($\delta^{13}C_a$) would emerge.

Temporal trends in SA($\delta^{13}C_a$) from the Scripps gap-filled data are not statistically different from zero, except at the tropical site Christmas Island and at the South Pole (Fig. 3). Averaging the trends across all eight sites yields -0.0038 ± 0.026 ‰ per century (mean $\pm$ 1 SD of the mean), and averaging the trends for the extratropical sites ALT, PTB, and LJO yields $+0.09 \pm 0.06$ ‰ per century, with both averaged trends not statistically different from zero. The trend for the NH extratropical sites translates into a change in SA($\delta^{13}C_a$) of around 5 ± 3 % over the 40-year observational period. For the fitted data, trends are statistically different from zero only at two sites (La Jolla and Christmas Island). This is consistent with Gonsamo et al. (2017), who did not detect a temporal trend in SA($\delta^{13}C_a$) and seasonal phasing by fitting Scripps daily flask data from the four sites of Alert, Nuvuk (formerly Point Barrow), La Jolla, and Mauna Loa. In summary, observed temporal trends in SA($\delta^{13}C_a$) are small (≤ 0.15 ‰per century) and are not statistically different from zero (at $p < 0.05$) at individual sites. A significant negative trend is found for the tropical site Christmas Island, and detection of trends is difficult at the Southern Hemisphere sites, where SA($\delta^{13}C_a$) is small.

Simulated trends in SA($\delta^{13}C_a$) are small (often less than 0.01 ‰ per decade) and statistically insignificant (5 % level) except at three SH sites (Ascension, Mahe, the South Pole) with a small seasonal cycle amplitude (Table 2). Observed relative trends in SA(C_a) are larger than in SA($\delta^{13}C_a$) in the northern high latitudes and are statistically significant at Alert, Nuvuk (formerly Point Barrow), Ocean Station, and Mahe Island but insignificant at all other sites over the 1982–2012 analysis period. Simulated trends in SA(C_a) are insignificant, except at four SH sites and on the Mariana Islands.

We compare model (m) and observed (o) slopes (β) to probe model–observation agreement. Under the null hypothesis of no slope difference, the $T = (\beta_m - \beta_o)/\sqrt{s^2_{\beta_m} + s^2_{\beta_o}}$ statistic (where s_β is the standard error in the β slope estimate) is Student's t distributed (Welch, 1947). Trends are different when the T values are larger than the 0.975 quantile of a t distribution with ν degrees of freedom ($T >\sim 2$). Modeled and observed trends are different at one site, the South Pole, for SA($\delta^{13}C_a$) and at one site (Nuvuk, formerly Point Barrow) for SA(C_a). As will become clear in the next section, the largest surface–atmosphere isotope fluxes and temporal changes in these fluxes are simulated in the region north of 40° N. We are therefore interested in quantifying how well the model represents temporal changes in SA(C_a) in this region and over a 40-year period, representative of the $\delta^{13}C_a$ observational record. For the five NH high-latitude sites with more than 20 years of data, uncertainties in the temporal changes in SA(C_a) range between 5 % and 13 % at individual sites over a 40-year period. The average trend in SA(C_a) for these five NH sites (Alert, Nuvuk (formerly Point Barrow), Ocean Station M, Cold Bay, Shemya Island) is 4.8 ± 1.6 ppm per century (31 ± 10 % per century) from observations and 3.8 ± 1.8 ppm per century (22 ± 11 % per century) from the model. These estimates translate into a relative change in SA(C_a) of around 4 % to 5 % over a 40-year period. This suggests that our model chain accurately represents the observed temporal changes in SA(C_a) in the NH extratropical atmosphere.

Given the mostly insignificant trends at individual sites over the model analysis period of 1982–2012, the question of whether larger trends are detected when considering longer timescales arises. Century-scale trends, or their absence, can be readily estimated in the simulations by comparing SA(C_a) and SA($\delta^{13}C_a$) for the modern period (1982–2012) (E_{standard}) and the preindustrial control (E_{control}) (Table 1; solid red versus dashed blue lines in Figs. S3 and S4). For C_a, a growth in SA is clearly visible (12.2 to 17.25 ppm at Alert, 6 to 8.3 ppm at Mauna Loa, 1.7 to 2.1 ppm at the South Pole). Across all 19 sites, SA(C_a) has grown by 44 % $\pm$ 35 % (mean $\pm$ standard deviation) from 1700 CE to 1982–2012. The growth in SA(C_a) ranges between 33 % and 42 % across the 12 extratropical NH sites (Table 1).

For $\delta^{13}C_a$, E_{control} and E_{standard} exhibit an almost identical SA averaged across all 19 sites (2 % $\pm$ 16 % lower in E_{control} than in E_{standard}). The change in SA($\delta^{13}C_a$) from the preindustrial (E_{control}) to modern (E_{standard}) periods ranges between -6 % and 9 % across the 12 extratropical NH sites, whereas more diverse results (-28 % to $+63$ %) are simulated at the tropical and SH sites (Fig. S4, Table 1). The change in SA($\delta^{13}C_a$), $S = E_{\text{standard}} - E_{\text{control}}$, does not emerge from the noise of variability ($N = 2$ standard deviations from IAV of E_{standard}), except at one tropical (Christmas Island) and three SH sites (Ascension Island, Mahe Island, Palmer Station); we require $|S|/N > 1$ for the signal S to emerge (Keller et al., 2014). The fact that trends in SA(C_a) and the near-zero trends in SA($\delta^{13}C_a$) are better identified by the difference between the modern and preindustrial periods than by regression over the modern period motivates us to focus on the comparison between E_{standard} versus E_{control} in the remaining result sections.

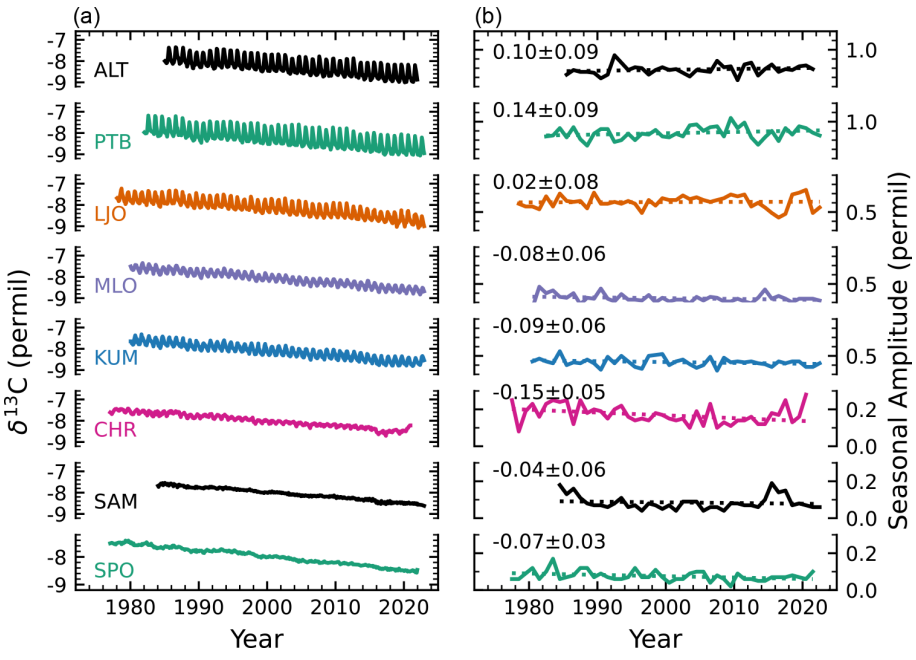

Figure 3. Temporal evolution of $\delta^{13}C_a$ **(a)** and its seasonal amplitude **(b)** from data of the Scripps network (Keeling et al., 2001). Gap-filled data provided by Scripps are used for the eight sites. The slope and its standard error from a linear regression through the seasonal amplitude data (dotted) are given in ‰ per century. Trends are not different from zero based on a two-sided t test and a significance level of 5 %, except at Christmas Island (CHR) and the South Pole (SPO). Sites are ordered according to latitude (Alert (ALT, 82° N), Nuvuk (formerly Point Barrow) (PTB, 71° N), La Jolla (LJO, 33° N), Mauna Loa Observatory (MLO, 20° N), Cape Kumukahi (KUM, 20° N), Christmas Island (CHR, 2° N), Samoa (SAM, 14° S), and the South Pole (SPO, 90° S)).

4.3 Zonal decomposition of seasonal land–biosphere fluxes

4.3.1 Changes in the seasonal amplitude of land–biosphere fluxes and $\delta^{13}C_a$ over the historical period

Next, we address the near-absent temporal trends in $SA(\delta^{13}C_a)$ at NH sites by analyzing the zonally averaged cumulative growing season flux of $|\delta^{13} f^*_{al,net}|$, i.e., $SA(\delta^{13} f^*_{al,net})$ (Fig. 4). The northern midlatitude to high-latitude ecosystem fluxes exhibit the largest seasonal cycle, followed by tropical rain-green forests and savannahs in $E_{standard}$. This flux pattern contributes to the larger $SA(\delta^{13}C_a)$ in the NH extratropics versus tropical and SH sites. A similar latitudinal flux pattern holds for $E_{control}$.

Turning to the change over the historical period, $SA(\delta^{13} f^*_{al,net})$ is 28 % larger for the region north of 15° N (30 % larger for > 40° N and 20 % larger for 15–40° N) for $E_{standard}$ than for $E_{control}$. This growth is comparable to the observed increase in C_a of 32 % from the preindustrial period to the reference period of 1982–2012. In contrast, $E_{control}$ sometimes exhibits larger $SA(\delta^{13} f^*_{al,net})$ than $E_{standard}$ in the tropical and SH ecosystems (Fig. 4). Following Eq. (8), the near-proportional growth in the $SA(\delta^{13} f^*_{al,net})$ and in annual mean C_a in the NH extratropics is consistent with the absence of any major long-term change in $SA(\delta^{13}C_a)$ at extratropical NH sites (Table 1 and Fig. S4). $SA(\delta^{13}C_a)$ and its change at extratropical NH sites is dominated by the large $SA(\delta^{13} f^*_{al,net})$ in the northern extratropics (Fig. 4), and transport from low-latitude regions is less important. On the other hand, the large extratropical $SA(\delta^{13} f^*_{al,net})$ influences $SA(\delta^{13}C_a)$ and its temporal changes at lower latitudes. Without this influence, we would, based on Eq. (8), expect a decrease in $SA(\delta^{13}C_a)$ outside the extratropics, given that the relative increase in annual mean C_a is larger than the increase in $SA(\delta^{13} f^*_{al,net})$ in these regions.

Factorial simulations with an individual forcing kept at preindustrial levels show small individual contributions by climate change, fossil fuel emissions, and land use to the industrial period growth in $SA(\delta^{13}C_a)$ at northern extratropical sites (Figs. S3 and S4). This suggests that the statistically insignificant trend in $SA(\delta^{13}C_a)$ at northern extratropical sites is not caused by offsetting impacts of climate change versus increasing C_a. Fossil fuel emissions cause an increase and land use change a reduction in $SA(\delta^{13}C_a)$ at low-latitude and southern sites (Figs. S3 and S4). We attribute the dampening influence of land use change to the replacement of C_4 plants by C_3 crops, causing a general shift in the fractionation during photosynthesis to less negative values south of ∼45° N (Fig. 4c). This damping influence highlights the importance of considering spatiotemporal variations in C_3

Table 2. Temporal trends in the seasonal cycle amplitude of C_a and $\delta^{13}C_a$ from the standard simulation ($E_{standard}$) and observations for 19 monitoring sites from 1982 to 2012. Observational data of C_a are from the GLOBALVIEW-CO_2 product and are fitted for the period of 1982–2012, while the data for $\delta^{13}C_a$ are from Scripps and are fitted as shown in Fig. 3. The seasonal cycle amplitude of a given year is only computed if at least 10 monthly values are available. The number of years included in the trend calculation for SA(C_a) and model-based SA($\delta^{13}C_a$) is given in parentheses. The observed trend for C_a is affected by anomalous values at Key Biscayne, which is not included. Over the period of 1982–2012, significant trends (two-sided t test at 5 % significance) are only found for Alert, Nuvuk (formerly Point Barrow), Ocean Station M, and Mahe Island for observed C_a; for Mariana Islands, Mahe Island, Palmer, Halley, and the South Pole for simulated C_a; and for Ascension, Mahe Island, and the South Pole for simulated $\delta^{13}C_a$. The decadal-scale trends are given per century for better readability.

	Trend in seasonal cycle amplitude			
	C_a [ppm per century]		$\delta^{13}C_a$ [‰ per century]	
Site	Observed	Model	Observed	Model (years)
Alert, Nunavut, Canada (82° N)	6.5 ± 2.3	5.3 ± 2.7	0.1 ± 0.09	0.02 ± 0.13 (25)
Nuvuk (formerly Point Barrow), Alaska, US (71° N)	9.5 ± 1.9	1.0 ± 3.6	0.14 ± 0.09	-0.09 ± 0.15 (26)
Ocean Station M, Norw. (66° N)	7.2 ± 3.1	7.7 ± 3.9		0.02 ± 0.17 (25)
Cold Bay, Alaska, US (55° N)	1.3 ± 4.4	5.2 ± 4.4		0.10 ± 0.20 (25)
Shemya Island, Alaska, US (53° N)	-0.5 ± 5.3	-0.4 ± 4.9		-0.04 ± 0.22 (21)
Mace Head, Ireland (53° N)	-9.6 ± 14.0	-5.6 ± 4.3		-0.27 ± 0.24 (15)
Terceira Island, Portugal (39° N)	-1.5 ± 6.6	5.7 ± 3.7		0.10 ± 0.17 (14)
Key Biscayne, Florida, US (26° N)		1.5 ± 1.7		0.03 ± 0.07 (25)
Mauna Loa, Hawaii, US (20° N)	-1.6 ± 1.0	0.6 ± 1.4	-0.08 ± 0.06	-0.07 ± 0.05 (26)
Cape Kumukahi, Hawaii, US (20° N)	-2.1 ± 2.0	2.2 ± 1.6	-0.09 ± 0.06	-0.01 ± 0.06 (26)
Mariana Islands, Guam (13° N)	-2.6 ± 4.8	4.1 ± 1.5		0.08 ± 0.05 (23)
Ragged Point, Barbados (13° N)	-2.1 ± 2.1	-0.3 ± 1.7		-0.06 ± 0.07 (18)
Christmas Island, Kiribati (2° N)	-2.4 ± 1.8	-1.9 ± 1.6	-0.15 ± 0.05	-0.13 ± 0.07 (19)
Mahe Island, Seychelles (5° S)	3.7 ± 1.4	6.4 ± 2.3		0.30 ± 0.07 (13)
Ascension Island, UK (7.6° S)	2.7 ± 1.8	-0.6 ± 1.4		-0.15 ± 0.05 (25)
Tutuila, American Samoa (14° S)	2.2 ± 1.3	-0.5 ± 0.9	-0.04 ± 0.06	-0.04 ± 0.02 (26)
Palmer Station, Antarctica (65° S)	-0.4 ± 0.9	2.4 ± 1.1		0.04 ± 0.04 (23)
Halley Station, Antarctica (76° S)	0.1 ± 1.8	2.9 ± 1.1		0.03 ± 0.04 (17)
South Pole, Antarctica (90° S)	0.7 ± 0.8	2.8 ± 0.7	-0.07 ± 0.03	0.06 ± 0.03 (26)

and C_4 plant distributions when analyzing $\delta^{13}C_a$. In summary, the results suggest that the near-proportional growth in SA($\delta^{13} f^*_{al,net}$) and in C_a is mainly responsible for the statistically insignificant trend in SA($\delta^{13}C_a$) at high-northern-latitude sites and contributes to the statistically insignificant trend in SA($\delta^{13}C_a$) at other NH sites via atmospheric transport.

For CO_2, the amplitude of the modeled zonally averaged net atmosphere-to-land CO_2 flux, SA($f_{al,net}$), shows the largest values in the NH extratropics and a large increase over the historical period of 33 % in the region 15–90° N (15–40° N – 26 %; 40–90° N – 37 %) driven by a larger increase in NPP than release fluxes (R), whereas SA($f_{al,net}$) is smaller in the tropics and SH and shows hardly any changes from the preindustrial ($E_{control}$) to modern ($E_{standard}$) periods south of 20° N. These results are consistent with previous studies showing northern ecosystems progressively taking up more carbon during the growing season (Graven et al., 2013; Forkel et al., 2016; Piao et al., 2018; Bastos et al., 2019). For example, using carbon fluxes from two atmospheric inversions and 11 land models, Bastos et al. (2019) find a positive trend in SA($f_{al,net}$) north of 40° N and small or no growth in SA($f_{al,net}$) between 25 and 40° N.

4.3.2 The coupling between the seasonal amplitude of C_a and $\delta^{13}C_a$

SA(C_a) and SA($\delta^{13}C_a$) are partly coupled by the underlying carbon fluxes. The question to which extent SA($\delta^{13}C_a$) holds information independent from SA(C_a) arises. We decompose $\delta^{13} f^*_{al,net}$ in a contribution linked to the net atmosphere-to-land carbon flux, $f_{al,net} = NPP - R$, and an isotopic disequilibrium flux (see Appendix A and Sect. 3 for notation; $f_{al,net}$ is positive for a flux into the land biosphere):

$$\delta^{13} f^*_{al,net} = \underbrace{(NPP - R)}_{f_{al,net}} \cdot \varepsilon_{NPP} - R \cdot \underbrace{\left(\delta^{13}C_R - \delta^{13}C_{NPP}\right)}_{\delta_{dis,la}}. \quad (9)$$

NPP is the net primary productivity of all plants within a grid cell. R is the sum of all land biosphere release fluxes to the atmosphere, such as those from heterotrophic respiration, fire, mortality, and product pools, except autotrophic respiration. $\delta^{13}C_R$ is the signature of R, and $\delta^{13}C_{NPP}$ is the signature

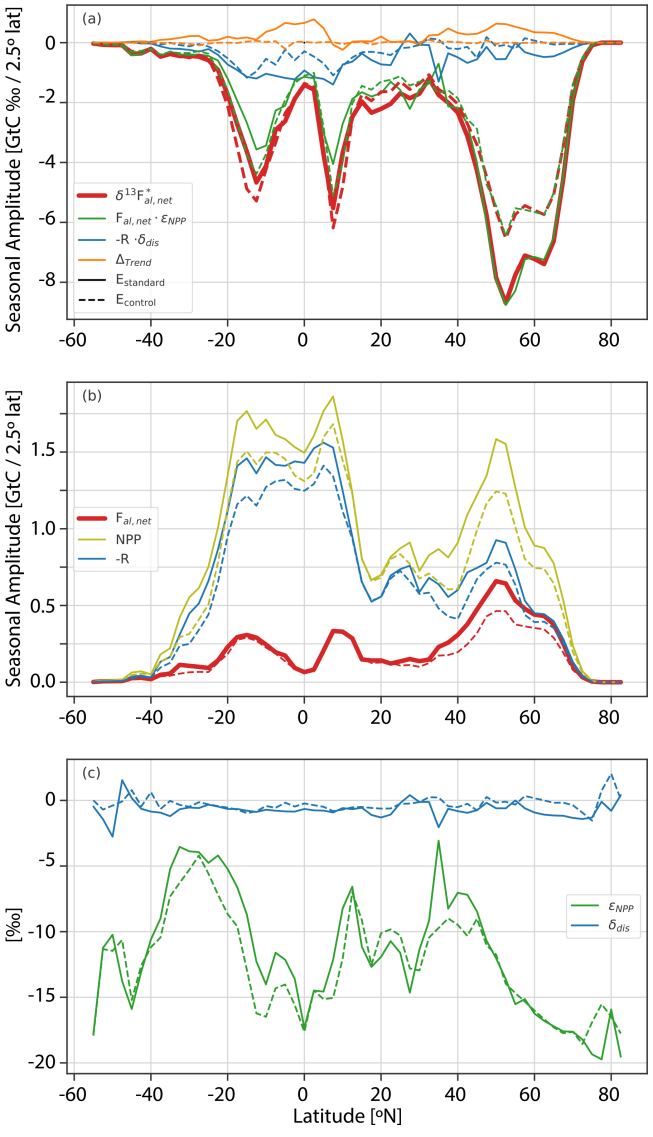

Figure 4. The seasonal amplitude per 2.5° latitude band of the signature-weighted, detrended net atmosphere–land flux, $\delta^{13} f^*_{\mathrm{al,net}}$, in the period of 1982–2012 is shown in **(a)** in red (see Eq. 8). This quantity is the sum of three constituent seasonal amplitudes (Eq. 9 and Appendix A): net land–atmosphere flux weighted with photosynthetic fractionation ($f_{\mathrm{al,net}} \cdot \varepsilon_{\mathrm{NPP}}$, green) plus release fluxes weighted with the disequilibrium signature ($R \cdot \delta_{\mathrm{dis,la}}$, blue) plus the contribution to the seasonal amplitude by the underlying trend of $\delta^{13} f^*_{\mathrm{al,net}}$ (Δ_{trend}, orange) (sign convention – green + blue + orange = red). In **(b)**, the seasonal amplitudes of (non-detrended) net carbon fluxes are shown. The net atmosphere–land flux ($f_{\mathrm{al,net}}$, red) is split into net primary productivity (NPP, olive) and release flux (R, blue). In **(c)** the corresponding fractionation of photosynthesis $\varepsilon_{\mathrm{NPP}}$ and the disequilibrium signature $\delta_{\mathrm{dis,la}}$ are shown. All values are for the period with $\delta^{13} f^*_{\mathrm{al,net}}$ smaller than zero (∼ growing season). The results from the standard simulation (E_{standard}, solid lines) are compared to the preindustrial control simulation (E_{control}, dashed lines).

of NPP, with $\varepsilon_{\mathrm{NPP}}$ (or $\varepsilon_{\mathrm{al}}$) representing the (flux-weighted) fractionation by NPP. The difference in signatures of R and NPP is the isotopic disequilibrium, $\delta_{\mathrm{dis,la}}$. Here, as in LPX-Bern, we have assumed that the uptake difference between gross primary production (GPP) and NPP is released on short timescales and without further carbon isotope fractionation.

Equation (9), together with Eqs. (7) and (8), provides insights into the driving factors for the seasonal amplitudes. Putting the ocean aside (Heimann et al., 1989), SA(C_a) is driven by the spatiotemporal pattern of NPP$-R$, whereas SA($\delta^{13}C_a$) is additionally influenced by seasonal variations in $\varepsilon_{\mathrm{NPP}}$, and the disequilibrium flux ($-R \cdot \delta_{\mathrm{dis,la}}$). The latter is indicative of the transit time of carbon through the land biosphere.

The decomposition of zonally averaged SA($\delta^{13} f^*_{\mathrm{al,net}}$) into the amplitude of constituent fluxes and their isotopic signatures is displayed in Fig. 4 and Table S1 in the Supplement. On the global average, SA($f_{\mathrm{al,net}} \cdot \varepsilon_{\mathrm{NPP}}$) contributes to SA($\delta^{13} f^*_{\mathrm{al,net}}$) with a fraction of 90 % for both E_{standard} and E_{control}. For the region north of 40° N, SA($-R \cdot \delta_{\mathrm{dis,la}}$) contributes only 7 % to SA($\delta^{13} f^*_{\mathrm{al,net}}$) in E_{standard} and is almost negligible in E_{control} (2 %). In E_{control}, SA($-R \cdot \delta_{\mathrm{dis,la}}$) and $\delta_{\mathrm{dis,la}}$, albeit to a smaller extent than in E_{standard}, are not negligible due to the lagged response of the respiration signatures to natural changes in $\varepsilon_{\mathrm{NPP}}$. A small contribution ($\Delta_{\mathrm{trend}}$) to the isotopic flux seasonality in E_{standard} arises from the long-term increase in flux (Fig. 4; see Appendix A). The small contribution of the disequilibrium flux ($-R \cdot \delta_{\mathrm{dis,la}}$) relative to the net flux ($f_{\mathrm{al,net}} \cdot \varepsilon_{\mathrm{NPP}}$; Eq. 9) arises as the seasonal amplitude of the carbon release flux R is similar in magnitude to that of the net land carbon uptake $f_{\mathrm{al,net}}$ in the northern extratropics (blue versus red lines in Fig. 4b), while the disequilibrium $\delta_{\mathrm{dis,la}}$ is an order of magnitude smaller than $\varepsilon_{\mathrm{NPP}}$ (Fig. 4c). Thus in LPX, SA($\delta^{13}C_a$) is dominated by the growing season net carbon uptake flux in northern high latitudes, suggesting that SA($\delta^{13}C_a$) holds little information on the isotopic disequilibrium at high-latitude sites. Rather, the additional information of SA($\delta^{13}C_a$) compared to SA(C_a) is on the magnitude of $\varepsilon_{\mathrm{NPP}}$ at northern high-latitude sites. In contrast, the contribution by the disequilibrium flux SA($-R \cdot \delta_{\mathrm{dis,la}}$) and the contribution by the net carbon flux SA($f_{\mathrm{al,net}} \cdot \varepsilon_{\mathrm{NPP}}$) are nearly equal in the tropics (10° S–10° N) and the SH (Fig. 4, Table S1), suggesting that SA($\delta^{13}C_a$) potentially holds additional information on R and carbon turnover in these regions in comparison to SA(C_a).

The zonal variation in (growing season) photosynthetic fractionation $\varepsilon_{\mathrm{NPP}}$ is mainly due to differences in vegetation composition, with C_4 plants having considerably lower photosynthetic fractionation than C_3 plants (Fig. 4c). Land use and the evolving distribution of C_3 and C_4 crops are prescribed in the model, and C_4 grasses are more prevalent than C_3 grasses in low-latitude dryland ecosystems. Accordingly, maxima in flux-weighted, zonal-mean $\varepsilon_{\mathrm{NPP}}$ are simulated at 35° N, 12° N, and broadly around 30° S. Minima are simulated for the C_3-dominated high-latitude ecosys-

tems and tropical rainforest zone. In E_{standard}, ε_{NPP} is generally less negative than in E_{control} and increased by 1.18 ‰ (9 % in relative units) on the global average (SA(NPP)-weighted), mainly due to the increase in the prevalence of C_4 plants, while ε_{NPP} remains time-invariant in the C_3-dominated ecosystems north of 45° N (Fig. 4c). To estimate the influence of the increase in C_4 prevalence on global mean ε_{NPP} (but not on global GPP), we run a factorial simulation, E_{C_3}, with the fractionation formulation for all C_4 plants replaced by that for C_3 plants. The difference between E_{standard} and E_{C_3}, i.e., the change in fractionation attributable to C_4 plants, amounts to about 1.5 ‰ on a global average (1982–2012 versus 1720–1750) (Fig. S5), pointing again to the importance of C_3 and C_4 plant distribution changes for $\delta^{13}C_a$.

Keeling et al. (2017) analyzed the atmospheric budgets of carbon and ^{13}C using seasonally detrended data, using a three-box land model with time-invariant overturning timescales, using globally uniform isotopic fractionation, and neglecting changes in C_3 and C_4 distribution in their standard setup. They found that global mean ε_{NPP} decreased by 0.66 ± 0.34 ‰ from 1975 to 2005 and attributed this change to changes in fractionation associated with mesophyll conductance and photorespiration of C_3 plants. It appears challenging to detect and attribute changes in the fractionation of global mean NPP with a box model, given uncertainties in NPP (Graven et al., 2024) and changes in C_3 versus C_4 plant distribution.

While the influence of the gross exchange flux and the isotopic disequilibrium on $\delta^{13}C_a$ seasonality is modeled to be small at northern sites of today, it remains to be explored how global warming will change these parameters, e.g., due to changes in fire frequency and tree mortality, and affect $\delta^{13}C_a$ and the information provided by continued $\delta^{13}C_a$ observations. We may also expect different disequilibrium fluxes and, in turn, $\delta^{13}C_a$ seasonality if the global carbon sink is driven by a stimulation of NPP, e.g., by CO_2 fertilization (Walker et al., 2021) as in LPX-Bern, versus a change in tree longevity (Bugmann and Christof, 2011; Körner, 2017). It remains to be investigated, e.g., by applying perturbed-parameter ensembles and sensitivity simulations, whether such differences indeed significantly affect $\delta^{13}C_a$ seasonality.

Monitoring C_a and $\delta^{13}C_a$ over tropical and SH land regions could potentially provide valid information to disentangle NPP, respiration, and net carbon fluxes, given the substantial contribution of the disequilibrium flux to SA($\delta^{13} f^*_{\text{al,net}}$). However, the seasonality of $\delta^{13}C_a$ and C_a at the tropical background monitoring sites analyzed in this study is strongly influenced by long-range transport, adding uncertainty to the interpretation of seasonal signals at background sites. Ideally, seasonally resolved observations are taken in air masses influenced primarily by regional land biosphere fluxes – thereby minimizing uncertainties from long-range transport – and interpreted with the help of atmospheric transport and land biosphere models (Botía et al., 2022). For example, the data may be assimilated into atmospheric transport models applied in inverse mode to infer surface carbon and isotope fluxes or assimilated into isotope-enabled land biosphere models combined with atmospheric transport to optimize parameters governing modeled carbon and isotope fluxes (Peylin et al., 2016; van der Velde et al., 2018; Castro-Morales et al., 2019).

4.4 Implications for stomatal conductance and water use

Our result of a time-invariant ε_{NPP} in northern extratropical regions holds implications for carbon and water fluxes and evaporative cooling. The good agreement between observations and model results for SA($\delta^{13}C_a$) and its temporal trend at northern sites provides implicit support for regulation of stomatal conductance by C_3 plants towards a constant ratio of the CO_2 mole fraction in the leaf intercellular space (c_i) and ambient atmospheric air (c_a) on the continental scale. Following Farquhar (1989) and Cernusak et al. (2013), ε_{NPP} is approximately proportional to c_i/c_a:

$$\varepsilon_{\text{NPP}} = -\left(a + (b-a)\cdot\frac{c_i}{c_a}\right), \tag{10}$$

with a (4.4) and b (27) being constants. Two contrasting scenarios are published for the regulation of leaf stomatal conductance for C_3 plants. First, many site studies (Voelker et al., 2016; Saurer et al., 2014; Kauwe et al., 2013; Peñuelas et al., 2011; Frank et al., 2015; Keller et al., 2017) suggest a regulation of stomatal conductance towards a constant c_i/c_a and, hence, suggest that c_i grows proportionally to c_a. An absent temporal trend in c_i/c_a translates into an absent trend in ε_{NPP} and vice versa (Eq. 10). Focusing on regions north of $> 40°$ N, where carbon fluxes are largest and C_3 plants dominate, LPX-Bern simulates a small role of isotopic disequilibrium fluxes and a dominant influence of net atmosphere–surface fluxes on SA($\delta^{13}C_a$) (Fig. 4, green versus blue lines). Importantly, LPX-Bern simulates small temporal changes in the (flux-weighted) fractionation of the zonally and seasonally integrated NPP at northern sites (Fig. 4c, green lines) and a stomatal regulation towards constant c_i/c_a. In turn, the good model–data agreement in the temporal trends of SA(C_a) and SA($\delta^{13}C_a$) implies consistency with the observational evidence for this scenario towards constant c_i/c_a.

In contrast, Battipaglia et al. (2013) and Keenan et al. (2013) suggest a regulation of stomatal conductance towards a constant c_i and a decreasing ratio of c_i/c_a under rising C_a. Evaluating Eq. (10) for 1980–2022, the period with $\delta^{13}C_a$ measurements, yields a decrease in ε_{NPP} of 15 % (−3.0 ‰ to −3.8 ‰) for an initial c_i/c_a ratio in the range of 0.7 to 0.9 and constant c_i. We argue that the good observation–model agreement in the simulated trends in SA(C_a) implies that the influence of the simulated net atmosphere–land carbon flux is realistic, and SA($\delta^{13}C_a$) would decrease if ε_{NPP} decreases.

A decrease in SA($\delta^{13}C_a$) of 15 % would emerge from the noise of variability at individual northern sites. Taken together, we suggest that the scenario towards constant c_i/c_a is consistent with the observations, whereas the scenario towards constant c_i appears less likely. However, uncertainties remain, and our conclusions for the two scenarios of stomatal regulation await confirmation by other modeling studies.

The two scenarios imply large differences in water fluxes (Knauer et al., 2017). The intrinsic water use efficiency (iWUE), the ratio between assimilation of CO_2 by photosynthesis (A) and conductance of CO_2 (g), is, as ε_{NPP}, a function of c_i and c_a:

$$\mathrm{iWUE} = \frac{A}{g} = c_a \cdot \left(1 - \frac{c_i}{c_a}\right). \tag{11}$$

iWUE would have increased from 1980 to 2022 by 23 % for constant c_i/c_a but by 77 % to 231 % for constant c_i, assuming an initial c_i/c_a of 0.7 to 0.9. In the latter scenario, stomatal conductance and correspondingly water loss per stomatal pore would have decreased strongly over the last decades.

Equation (10) is an approximation (Farquhar et al., 1982; Lloyd and Farquhar, 1994; Farquhar and Cernusak, 2012; Cernusak et al., 2013) considered to be sufficient for many applications by Cernusak et al. (2013) and applied in the publications cited in the previous two paragraphs. However, there are four contributions only implicitly considered by choosing parameter b in Eq. (10), and these may contribute small temporal trends to ε_{NPP}. In turn, inferred c_i/c_a would also have a temporal trend for a constant ε_{NPP}. We estimate the trend contribution of these additional terms to be of small magnitude (< 1 ‰) in comparison to the 3 ‰ to 3.8 ‰ difference estimated for our two scenarios (see Appendix B for details).

5 Conclusions

We explored the global-scale mechanisms driving the observed seasonal cycles of $\delta^{13}C$ of atmospheric CO_2 ($\delta^{13}C_a$) and of atmospheric CO_2 at 19 monitoring sites using atmosphere–surface fluxes from the Bern3D-LPX Earth system model of intermediate complexity and fossil fuel emissions in combination with transport matrices from the TM3 atmospheric transport model. We find good data–model agreement at northern and tropical sites. No significant trends are detected or modeled in the seasonal cycle amplitude of $\delta^{13}C_a$ at most monitoring sites, in contrast to the positive trends in the seasonal amplitude of CO_2. We attribute the statistically insignificant trend in the seasonal amplitude of $\delta^{13}C_a$ to a near-equal percentage increase in the growing season net carbon uptake and isotope flux and in the background atmospheric CO_2 in the northern extratropical land regions. Over the industrial period and at low-latitude and SH sites, land use change has a dampening influence on $\delta^{13}C_a$ seasonality through the replacement of C_3 plants by C_4 crops. Modeled isotopic disequilibrium fluxes have a small influence on the seasonal signal of $\delta^{13}C_a$ at NH sites but play an important role in tropical and SH ecosystems, suggesting that monitoring the $\delta^{13}C_a$ seasonality over tropical and SH land would provide valuable information on gross carbon exchange fluxes and the timescales of carbon turnover in the land biosphere. Our results, based on a single model chain, provide implicit support for a regulation of the stomatal conductance of C_3 plants towards a constant c_i/c_a ratio on biome scales and for intrinsic water use efficiency to grow proportionally to atmospheric CO_2 over recent decades, with implications for carbon and water fluxes. More generally, the results suggest that observations of the $\delta^{13}C_a$ seasonal cycle offer highly useful information on carbon and water cycle processes. We recommend seasonally resolved $\delta^{13}C_a$ observations as a constraint for land biosphere models used to simulate the terrestrial sink of anthropogenic carbon and land use emissions, for example, using perturbed parameter ensembles in Bayesian approaches (Lienert and Joos, 2018; van der Velde et al., 2018). Future studies may employ an ensemble of isotope-enabled models and perturbed parameter ensembles to elucidate whether our findings are robust and to show which models or process assumptions are compatible or incompatible with $\delta^{13}C_a$ data for improved projections of atmospheric CO_2 and global warming.

Appendix A: Decomposition of $\delta^{13} f^*_{as,net}$ and the calculation of seasonal amplitudes

We reformulate the net isotope flux in terms of net and gross carbon fluxes, isotopic fractionation, and isotopic disequilibrium (e.g., Mook, 1986; Joos and Bruno, 1998) to diagnose their influence on the seasonal cycles.

The fractionation for a gross flux, e.g., from the atmosphere to the surface, is

$$\varepsilon_{as} \cong (\delta^{13}C_{as} - \delta^{13}C_a), \tag{A1}$$

with $\delta^{13}C_{as}$ the signature of the gross flux from a to s (f_{as}) and $\delta^{13}C_a$ the signature of the source. The isotopic disequilibrium (or difference) between atmosphere–surface gross fluxes is

$$\delta_{dis,sa} = -\delta_{dis,as} = \left(\delta^{13}C_{sa} - \delta^{13}C_{as}\right). \tag{A2}$$

The net carbon and isotope fluxes are the differences between the gross fluxes:

$$f_{as,net} = f_{as} - f_{sa} \tag{A3}$$

$$\delta^{13} f^*_{as,net} = f_{as} \cdot \left(\delta^{13}C_{as} - \delta^{13}C_a\right) - f_{sa} \cdot \left(\delta^{13}C_{sa} - \delta^{13}C_a\right). \tag{A4}$$

Rearranging yields

$$\delta^{13} f^*_{\mathrm{as,net}} = f_{\mathrm{as,net}} \cdot \underbrace{\left(\delta^{13}\mathrm{C_{as}} - \delta^{13}\mathrm{C_a}\right)}_{\varepsilon_{\mathrm{as}}} - f_{\mathrm{sa}} \cdot \underbrace{\left(\delta^{13}\mathrm{C_{sa}} - \delta^{13}\mathrm{C_{as}}\right)}_{\delta_{\mathrm{dis,sa}}}. \quad \text{(A5)}$$

For the land biosphere (l), it follows from Eqs. (A3) and (A5) that

$$f_{\mathrm{al,net}} = \mathrm{NPP} - R \quad \text{(A6)}$$

$$\delta^{13} f^*_{\mathrm{al,net}} = f_{\mathrm{al,net}} \cdot \varepsilon_{\mathrm{NPP}} - R \cdot \delta_{\mathrm{dis,la}}, \quad \text{(A7)}$$

with

$$\delta_{\mathrm{dis,la}} = \delta^{13}\mathrm{C}_R - \delta^{13}\mathrm{C_{NPP}}. \quad \text{(A8)}$$

NPP is the net primary productivity of all plants within a grid cell. R is the sum of all release fluxes to the atmosphere, such as those from heterotrophic respiration, fire, mortality, and product pools, except autotrophic respiration. $\delta^{13}C_R$ is the signature of R, and $\delta^{13}C_{\mathrm{NPP}}$ is the signature of NPP, with $\varepsilon_{\mathrm{NPP}}$ (or $\varepsilon_{\mathrm{al}}$) representing the (flux-weighted) fractionation by NPP.

The seasonal amplitudes of $\delta^{13} f^*_{\mathrm{al,net}}$ and its components are calculated as follows. The time series of $\delta^{13} f^*_{\mathrm{al,net}}$ is detrended and normalized to zero. The trend is computed by a rolling 12-month mean of $\delta^{13} f^*_{\mathrm{al,net}}$. Then, the resulting trend curve is subtracted from $\delta^{13} f^*_{\mathrm{al,net}}$ (disregarding the first and last 6 months of the original series) to get a detrended curve. Finally, the detrended curve is normalized by subtracting its period mean. Δ_{trend} (e.g., in units of mol ‰ yr^{-1} m^{-2}) is the difference between $\delta^{13} f^*_{\mathrm{al,net}}$ after and before this detrending and normalizing procedure. We define a seasonal mask to compute seasonal amplitudes of fluxes and their signatures. For each model year, we identify months in which detrended $\delta^{13} f^*_{\mathrm{al,net}}$ is negative or equal to zero (roughly corresponding to the growing season). The sum of fluxes of these months is then termed the seasonal amplitude in a given year. For $\delta^{13} f^*_{\mathrm{al,net}}$, this procedure is consistent with considering the difference between maximum and minimum values of the detrended cumulative sum of $\delta^{13} f^*_{\mathrm{al,net}}$. Accordingly, the seasonal amplitudes of the component fluxes contributing to $\delta^{13} f^*_{\mathrm{al,net}}$ are computed by summation over months where $\delta^{13} f^*_{\mathrm{al,net}}$ is less than or equal to zero within a given year. Component fluxes are $[(\mathrm{NPP}-R)\cdot\varepsilon_{\mathrm{NPP}}]$, $[R\cdot\delta_{\mathrm{dis,la}}]$, $[\Delta_{\mathrm{trend}}]$ and, further, [NPP], $[R]$, and $[\mathrm{NPP}-R]$ (Fig. 4). These component fluxes are not detrended to readily calculate the signatures $\delta_{\mathrm{dis,la}}$ and $\varepsilon_{\mathrm{NPP}}$ by division of the seasonal amplitude isotopic flux with the corresponding seasonal amplitude carbon flux.

We note that the annual climatological mean values of the isotopic disequilibrium ($\delta_{\mathrm{dis,la}}$), the net carbon flux ($f_{\mathrm{al,net}}$), and the net isotopic flux ($\delta^{13} f^*_{\mathrm{al,net}}$) vanish by definition for the preindustrial equilibrium. However, this does not hold for their seasonal amplitudes. Further, detrending $\delta^{13} f^*_{\mathrm{al,net}}$ before the computation of its seasonal amplitude is consistent with the calculation of the C_a and $\delta^{13}C_a$ seasonal amplitude from the detrended atmospheric time series.

The seasonal cycles of C_a or $\delta^{13}C_a$ are computed from observations and the TM3 results using the following procedure for either C_a or $\delta^{13}C_a$. Months with missing values in either the observations or the TM3 simulation are masked in the TM3 and observational time series. Then the time series are detrended using a 12-month rolling mean, and the overall mean of the series is set to zero to get (for year, y, and month, m) seasonal anomalies $\Delta C_a(y,m)$ and $\Delta\delta^{13}C_a(y,m)$. Finally, the period means for each calendar month, $\overline{\Delta C_a(m)}$ and $\overline{\Delta\delta^{13}C_a(m)}$, are computed by averaging over all corresponding monthly values. Additionally, the standard deviation is computed for each calendar month to inform about the interannual variability in the seasonality. The period-mean SA is computed as the difference between the month with the highest ($\overline{m_{\max}}$) and lowest ($\overline{m_{\min}}$) value in $\overline{\Delta C_a(m)}$ and $\overline{\Delta\delta^{13}C_a(m)}$, respectively. For individual years, we computed SA by the difference from the extreme monthly values of each year.

Appendix B: Uncertainties in the relationship between $\varepsilon_{\mathrm{NPP}}$ and c_i/c_a

In Sect. 4.4, we applied a simplified expression for fractionation of C_3 plants during photosynthesis ($\varepsilon_{\mathrm{NPP}}$) and used this expression to translate trends in $\varepsilon_{\mathrm{NPP}}$ to trends in c_i/c_a and in iWUE. The potential contributions to trends in $\varepsilon_{\mathrm{NPP}}$ from neglected ternary effects, dark-day respiration, and transport through the mesophyll and photorespiration are discussed in this appendix.

The isotopic fraction for C_3 photosynthesis is framed as a multi-step process considering the transport of CO_2 and the underlying gradients in CO_2 mole fractions from the ambient air (mole fraction – c_a) to the leaf surface (c_s) in the intercellular air spaces (c_i) and the sites of carboxylation (c_c), as well as the fractionation during carboxylation, dark-day respiration, R_d, and photorespiration (Cernusak, 2013). The transport of CO_2 equals the consumption of CO_2 by assimilation, A: $A = g(c_a - c_i) = g_m(c_i - c_c)$, with g being the conductance of the stomatal pores and the boundary layer and g_m the mesophyll conductance. The relationship can be rewritten as $A/(g\,c_a) = (1 - c_i/c_a) = g_m/g\,(c_i/c_a - c_c/c_a)$. If A increases in proportion to c_a and g and g_m is assumed to be constant, then it follows that c_i/c_a and c_c/c_a are also constant. In turn, the fractionation associated with the boundary layer and stomatal conductance ($-a(1 - c_i/c_a)$; $a = 4.4$ ‰), mesophyll conductance ($-a_m(c_i/c_a - c_c/c_a)$; $a_m = 1.8$ ‰), and carboxylation ($-b \times c_c$) remain constant. The overall in-

fluence of mesophyll transport on ε_{NPP} can also be written as $(b - a_m)/g_m \times A/c_a$ (Keeling et al., 2017).

Keeling et al. (2017) assumed that A/c_a decreases over time, with A increasing by 45 % for a doubling of CO_2, and that therefore fractionation by the mesophyll contribution would change by $-0.006\,‰\,ppm^{-1}$, i.e., a change in ε_{NPP} of 0.47 ‰ for the CO_2 increase of 78 ppm from 1980 to 2022. On the other hand, Campbell et al. (2017) observationally constrained the growth in gross primary production over the 20th century to be 31 ± 5 %, larger than the increase in c_a of 25 %. Accordingly, A/c_a increases, and the mesophyll trend contribution is positive. With the central parameter values of Keeling et al. (2017) ($A = 9\,\mu mol\,m^{-2}\,s^{-1}$, $g_m = 0.2\,mol\,m^{-2}\,s^{-1}$, $CO_2 = 355$ ppm), the contribution is $+0.002\,‰\,ppm^{-1}$. Keeling et al. (2017) also estimated changes in fractionation associated with photorespiration ($-f \times \Gamma^*/c_a$; $f = 12\,‰$) to be $-0.004\,‰\,ppm^{-1}$ assuming a constant CO_2 compensation point, Γ^*. The real sensitivity must be smaller, as Γ^* increases with temperature and because Keeling et al. (2017) applied an estimate for the CO_2 compensation point in the presence of R_d (43 ppm) instead of the absence of R_d ($\Gamma^* = 31$ ppm). Further, fractionation during day respiration is $-e \times c_c/c_a \times R_d/V_c$ (Cernusak et al., 2013), roughly about 0 to $-0.3\,‰$ for e in the range of 0 ‰ to 5 ‰; we apply RuBisCO carboxylation rates, V_c, of $11\,\mu mol\,m^{-2}\,s^{-1}$ derived from the value of $A = 9\,\mu mol\,m^{-2}\,s^{-1}$ by Keeling et al. (2017), ($R_d = 1\,\mu mol\,m^{-2}\,s^{-1}$ and $c_c/c_a = 0.6$). Finally, ternary effects of about $-0.7\,‰$ ($0.024 \times b$) increase with water vapor deficit (Farquhar and Cernusak, 2012). Given the small amplitudes of these two contributions, their temporal trends have also been small over recent decades.

Code and data availability. The data from the Scripps CO_2 program are available here: https://scrippsco2.ucsd.edu/data/atmospheric_co2/ (last access: 17 April 2023, Keeling et al., 2001). The GLOBALVIEW data from the NOAA Global Monitoring Laboratory were downloaded here: https://gml.noaa.gov/ccgg/globalview/ (last access: 27 April 2022, Cooperative Global Atmospheric Data Integration Project, 2013). The model data displayed in the figures and plotting scripts are available here: https://zenodo.org/records/14051464 (last access: 7 November 2024, https://doi.org/10.5281/zenodo.14051464, Joos et al., 2024).

Supplement. The supplement related to this article is available online at: https://doi.org/10.5194/bg-22-19-2025-supplement.

Author contributions. FJ and SL wrote the paper with inputs from SZ. SL performed all model runs, and FJ did the statistical analyses. SL and FJ produced the figures and tables.

Competing interests. The contact author has declared that none of the authors has any competing interests.

Disclaimer. The work reflects only the authors' view; the European Commission and their executive agency are not responsible for any use that may be made of the information the work contains.

Publisher's note: Copernicus Publications remains neutral with regard to jurisdictional claims made in the text, published maps, institutional affiliations, or any other geographical representation in this paper. While Copernicus Publications makes every effort to include appropriate place names, the final responsibility lies with the authors.

Acknowledgements. We thank the researchers of the Cooperative Atmospheric Data Integration Project, NOAA Earth System Research Laboratories (ESRL), Boulder, Colorado, and of the Scripps CO_2 program for making their CO_2 and $\delta^{13}C$ data freely available. We also thank Martin Heimann for suggesting that we plot seasonal anomalies of CO_2 versus those of $\delta^{13}C$. A special thanks goes to Christoph Köstler for providing the TM3 transport matrices and to Aurich Jeltsch-Thömmes for help with Bern3D. We thank Gerbrand Koren and an anonymous reviewer for their careful reviews and Ji-Hyung Park for editing the paper.

Financial support. This project has received funding from the European Union's Horizon 2020 research and innovation program under grant agreement no. 821003 (project 4C, Climate–Carbon Interactions in the Current Century) and from the Swiss National Science Foundation (project no. 200020_200511).

Review statement. This paper was edited by Ji-Hyung Park and reviewed by Gerbrand Koren and one anonymous referee.

References

Andres, R., Marland, G., Boden, T., and Bischof, S.: Carbon dioxide emissions from fossil fuel consumption and cement manufacture, 1751–1991, and an estimate of their isotopic composition and latitudinal distribution, in: The Carbon Cycle, edited by: Wigley, T. M. L. and Schimmel, D., Cambridge University Press, New York, USA, 53–62, ISBN 0 521 58337 3, 2000.

Andres, R., Boden, T., and Marland, G.: Monthly Fossil-Fuel CO_2 Emissions: Mass of Emissions Gridded by One Degree Latitude by One Degree Longitude – 2016, ESS-DIVE [data set], https://doi.org/10.3334/CDIAC/FFE.MONTHLYMASS.2016, 2009a.

Andres, R., Boden, T., and Marland, G.: Monthly Fossil-Fuel CO_2 Emissions: Isomass of Emissions Gridded by One Degree Latitude by One Degree Longitude, ESS-DIVE [data set], https://data.ess-dive.lbl.gov/view/doi:10.3334/CDIAC/FFE.MONTHLYISOMASS.2016 (last access: 23 December 2024), 2009b.

Andres, R., Boden, T., and Marland, G.: Annual Fossil-Fuel CO_2 Emissions: Global Stable Carbon Isotopic Signature, ESS-DIVE [data set], https://doi.org/10.3334/CDIAC/FFE.DB1013.2017, 2017.

Bacastow, R. B., Keeling, C. D., and Whorf, T. P.: Seasonal amplitude increase in atmospheric CO_2 concentration at Mauna Loa, Hawaii, 1959–1982, J. Geophys. Res.-Atmos., 90, 10529–10540, https://doi.org/10.1029/JD090iD06p10529, 1985.

Ballantyne, A. P., Miller, J. B., and Tans, P. P.: Apparent seasonal cycle in isotopic discrimination of carbon in the atmosphere and biosphere due to vapor pressure deficit, Global Biogeochem. Cy., 24, 1–16, https://doi.org/10.1029/2009GB003623, 2010.

Ballantyne, A. P., Miller, J. B., Baker, I. T., Tans, P. P., and White, J. W. C.: Novel applications of carbon isotopes in atmospheric CO_2: what can atmospheric measurements teach us about processes in the biosphere?, Biogeosciences, 8, 3093–3106, https://doi.org/10.5194/bg-8-3093-2011, 2011.

Barlow, J. M., Palmer, P. I., Bruhwiler, L. M., and Tans, P.: Analysis of CO_2 mole fraction data: first evidence of large-scale changes in CO_2 uptake at high northern latitudes, Atmos. Chem. Phys., 15, 13739–13758, https://doi.org/10.5194/acp-15-13739-2015, 2015.

Bastos, A., Ciais, P., Chevallier, F., Rödenbeck, C., Ballantyne, A. P., Maignan, F., Yin, Y., Fernández-Martínez, M., Friedlingstein, P., Peñuelas, J., Piao, S. L., Sitch, S., Smith, W. K., Wang, X., Zhu, Z., Haverd, V., Kato, E., Jain, A. K., Lienert, S., Lombardozzi, D., Nabel, J. E. M. S., Peylin, P., Poulter, B., and Zhu, D.: Contrasting effects of CO_2 fertilization, land-use change and warming on seasonal amplitude of Northern Hemisphere CO_2 exchange, Atmos. Chem. Phys., 19, 12361–12375, https://doi.org/10.5194/acp-19-12361-2019, 2019.

Battaglia, G. and Joos, F.: Marine N_2O Emissions From Nitrification and Denitrification Constrained by Modern Observations and Projected in Multimillennial Global Warming Simulations, Global Biogeochem. Cy., 32, 92–121, https://doi.org/10.1002/2017GB005671, 2018.

Battipaglia, G., Saurer, M., Cherubini, P., Calfapietra, C., McCarthy, H. R., Norby, R. J., and Francesca Cotrufo, M.: Elevated CO_2 increases tree-level intrinsic water use efficiency: insights from carbon and oxygen isotope analyses in tree rings across three forest FACE sites, New Phytol., 197, 544–554, https://doi.org/10.1111/nph.12044, 2013.

Becker, M., Steinhoff, T., and Körtzinger, A.: A Detailed View on the Seasonality of Stable Carbon Isotopes Across the North Atlantic, Global Biogeochem. Cy., 32, 1406–1419, https://doi.org/10.1029/2018GB005905, 2018.

Botía, S., Komiya, S., Marshall, J., Koch, T., Gałkowski, M., Lavric, J., Gomes-Alves, E., Walter, D., Fisch, G., Pinho, D. M., Nelson, B. W., Martins, G., Luijkx, I. T., Koren, G., Florentie, L., Carioca de Araújo, A., Sá, M., Andreae, M. O., Heimann, M., Peters, W., and Gerbig, C.: The CO_2 record at the Amazon Tall Tower Observatory: A new opportunity to study processes on seasonal and inter-annual scales, Glob. Change Biol., 28, 588–611, https://doi.org/10.1111/gcb.15905, 2022.

Bugmann, H. and Christof, B.: Will the CO_2 fertilization effect in forests be offset by reduced tree longevity?, Oecologia, 165, 533–544, https://doi.org/10.1007/s00442-010-1837-4, 2011.

Campbell, J. E., Berry, J. A., Seibt, U., Smith, S. J., Montzka, S. A., Launois, T., Belviso, S., Bopp, L., and Laine, M.: Large historical growth in global terrestrial gross primary production, Nature, 544, 84–87, 2017.

Castro-Morales, K., Schürmann, G., Köstler, C., Rödenbeck, C., Heimann, M., and Zaehle, S.: Three decades of simulated global terrestrial carbon fluxes from a data assimilation system confronted with different periods of observations, Biogeosciences, 16, 3009–3032, https://doi.org/10.5194/bg-16-3009-2019, 2019.

Cernusak, L. A. and Ubierna, N.: Carbon Isotope Effects in Relation to CO_2 Assimilation by Tree Canopies, 291–310, Springer International Publishing, Cham, ISBN 978-3-030-92698-4, https://doi.org/10.1007/978-3-030-92698-4_9, 2022.

Cernusak, L. A., Ubierna, N., Winter, K., Holtum, J. A. M., Marshall, J. D., and Farquhar, G. D.: Environmental and physiological determinants of carbon isotope discrimination in terrestrial plants, New Phytol., 200, 950–965, https://doi.org/10.1111/nph.12423, 2013.

Cooperative Global Atmospheric Data Integration Project: Multi-laboratory compilation of synchronized and gap-filled atmospheric carbon dioxide records for the period 1979–2012 (obspack_co2_1_GLOBALVIEW-CO2_2013_v1.0.4_2013-12-23), NOAA Global Monitoring Laboratory [data set], https://doi.org/10.3334/OBSPACK/1002, 2013.

Craig, H.: Isotopic standards for carbon and oxygen and correction factors for mass-spectrometric analysis of carbon dioxide, Geochim. Cosmochim. Ac., 12, 133–149, https://doi.org/10.1016/0016-7037(57)90024-8, 1957.

Dargaville, R. J., Heimann, M., McGuire, A. D., Prentice, I. C., Kicklighter, D. W., Joos, F., Clein, J. S., Esser, G., Foley, J., Kaplan, J., Meier, R. A., Melillo, J. M., Moore, B., Ramankutty, N., Reichenau, T., Schloss, A., Sitch, S., Tian, H., Williams, L. J., and Wittenberg, U.: Evaluation of terrestrial carbon cycle models with atmospheric CO_2 measurements: Results from transient simulations considering increasing CO_2, climate, and land-use effects, Global Biogeochem. Cy., 16, 39-1–39-15, https://doi.org/10.1029/2001gb001426, 2002.

Farquhar, G.: Carbon Isotope Discrimination And Photosynthesis, Annu. Rev. Plant Phys., 40, 503–537, https://doi.org/10.1146/annurev.arplant.40.1.503, 1989.

Farquhar, G. and Cernusak, L.: Ternary effects on the gas exchange of isotopologues of carbon dioxide, Plant Cell Environ., 35, 1221–1231, https://doi.org/10.1111/j.1365-3040.2012.02484.x, 2012.

Farquhar, G. D., O'Leary, M. H., and Berry, J. A.: On the relationship between carbon isotope discrimination and the intercellular carbon dioxide concentration in leaves, Aust. J. Plant Physiol., 9, 121–137, 1982.

Fay, A. R., Gregor, L., Landschützer, P., McKinley, G. A., Gruber, N., Gehlen, M., Iida, Y., Laruelle, G. G., Rödenbeck, C., Roobaert, A., and Zeng, J.: SeaFlux: harmonization of air–sea CO_2 fluxes from surface pCO_2 data products using a standardized approach, Earth Syst. Sci. Data, 13, 4693–4710, https://doi.org/10.5194/essd-13-4693-2021, 2021.

Forkel, M., Carvalhais, N., Rödenbeck, C., Keeling, R., Heimann, M., Thonicke, K., Zaehle, S., and Reichstein, M.: Enhanced seasonal CO_2 exchange caused by amplified plant productivity in northern ecosystems, Science, 351, 696–699, https://doi.org/10.1126/science.aac4971, 2016.

Frank, D. C., Poulter, B., Saurer, M., Esper, J., Huntingford, C., Helle, G., Treydte, K., Zimmermann, N. E., Schleser, G. H.,

Ahlstrom, A., Ciais, P., Friedlingstein, P., Levis, S., Lomas, M., Sitch, S., Viovy, N., Andreu-Hayles, L., Bednarz, Z., Berninger, F., Boettger, T., D/'Alessandro, C. M., Daux, V., Filot, M., Grabner, M., Gutierrez, E., Haupt, M., Hilasvuori, E., Jungner, H., Kalela-Brundin, M., Krapiec, M., Leuenberger, M., Loader, N. J., Marah, H., Masson-Delmotte, V., Pazdur, A., Pawelczyk, S., Pierre, M., Planells, O., Pukiene, R., Reynolds-Henne, C. E., Rinne, K. T., Saracino, A., Sonninen, E., Stievenard, M., Switsur, V. R., Szczepanek, M., Szychowska-Krapiec, E., Todaro, L., Waterhouse, J. S., and Weigl, M.: Water-use efficiency and transpiration across European forests during the Anthropocene, Nat. Clim. Change, 5, 579–583, 2015.

Friedlingstein, P., O'Sullivan, M., Jones, M. W., Andrew, R. M., Hauck, J., Olsen, A., Peters, G. P., Peters, W., Pongratz, J., Sitch, S., Le Quéré, C., Canadell, J. G., Ciais, P., Jackson, R. B., Alin, S., Aragão, L. E. O. C., Arneth, A., Arora, V., Bates, N. R., Becker, M., Benoit-Cattin, A., Bittig, H. C., Bopp, L., Bultan, S., Chandra, N., Chevallier, F., Chini, L. P., Evans, W., Florentie, L., Forster, P. M., Gasser, T., Gehlen, M., Gilfillan, D., Gkritzalis, T., Gregor, L., Gruber, N., Harris, I., Hartung, K., Haverd, V., Houghton, R. A., Ilyina, T., Jain, A. K., Joetzjer, E., Kadono, K., Kato, E., Kitidis, V., Korsbakken, J. I., Landschützer, P., Lefèvre, N., Lenton, A., Lienert, S., Liu, Z., Lombardozzi, D., Marland, G., Metzl, N., Munro, D. R., Nabel, J. E. M. S., Nakaoka, S.-I., Niwa, Y., O'Brien, K., Ono, T., Palmer, P. I., Pierrot, D., Poulter, B., Resplandy, L., Robertson, E., Rödenbeck, C., Schwinger, J., Séférian, R., Skjelvan, I., Smith, A. J. P., Sutton, A. J., Tanhua, T., Tans, P. P., Tian, H., Tilbrook, B., van der Werf, G., Vuichard, N., Walker, A. P., Wanninkhof, R., Watson, A. J., Willis, D., Wiltshire, A. J., Yuan, W., Yue, X., and Zaehle, S.: Global Carbon Budget 2020, Earth Syst. Sci. Data, 12, 3269–3340, https://doi.org/10.5194/essd-12-3269-2020, 2020.

GLOBALVIEW-CO2C13: Cooperative Atmospheric Data Integration Project – d13C of Carbon Dioxide, CD-ROM, NOAA ESRL, Boulder, Colorado, USA, 2009.

Gonsamo, A., D'Odorico, P., Chen, J. M., Wu, C., and Buchmann, N.: Changes in vegetation phenology are not reflected in atmospheric CO_2 and $^{13}C/^{12}C$ seasonality, Glob. Change Biol., 23, 4029–4044, https://doi.org/10.1111/gcb.13646, 2017.

Graven, H. D., Keeling, R. F., Piper, S. C., Patra, P. K., Stephens, B. B., Wofsy, S. C., Welp, L. R., Sweeney, C., Tans, P. P., Kelley, J. J., Daube, B. C., Kort, E. A., Santoni, G. W., and Bent, J. D.: Enhanced Seasonal Exchange of CO_2 by Northern Ecosystems Since 1960, Science, 341, 1085–1089, https://doi.org/10.1126/science.1239207, 2013.

Graven, H. D., Warren, H., Gibbs, H. K., Khatiwala, S., Koven, C., Lester, J., Levin, I., Spawn-Lee, S. A., and Wieder, W.: Bomb radiocarbon evidence for strong global carbon uptake and turnover in terrestrial vegetation, Science, 384, 1335–1339, https://doi.org/10.1126/science.adl4443, 2024.

Gurney, K. R., Law, R. M., Denning, A. S., Rayner, P. J., Pak, B. C., Baker, D., Bousquet, P., Bruhwiler, L., Chen, Y.-H., Ciais, P., Fung, I. Y., Heimann, M., John, J., Maki, T., Maksyutov, S., Peylin, P., Prather, M., and Taguchi, S.: Transcom 3 inversion intercomparison: Model mean results for the estimation of seasonal carbon sources and sinks, Global Biogeochem. Cy., 18, GB1010, https://doi.org/10.1029/2003GB002111, 2004.

Harris, I., Osborn, T. J., Jones, P., and Lister, D.: Version 4 of the CRU TS monthly high-resolution gridded multivariate climate dataset, Sci. Data, 7, 1–18, https://doi.org/10.1038/s41597-020-0453-3, 2020.

Hauck, J. and Völker, C.: Rising atmospheric CO_2 leads to large impact of biology on Southern Ocean CO_2 uptake via changes of the Revelle factor, Geophys. Res. Lett., 42, 1459–1464, https://doi.org/10.1002/2015GL063070, 2015.

Heimann, M. and Körner, S.: The Global Atmospheric Tracer Model TM3, Technical Reports, Max-Planck-Institut für Biogeochemie, Max-Planck-Institut für Biogeochemie, Jena (Germany), Vol. 5, https://www.bgc-jena.mpg.de/archived/, (last access: 23 December 2024), 2003.

Heimann, M., Keeling, C. D., and Tucker, C. J.: A three dimensional model of atmospheric CO_2 transport based on observed winds: 3. Seasonal cycle and synoptic time scale variations, in: Aspects of Climate Variability in the Pacific and the Western Americas, 277–303, American Geophysical Union (AGU), ISBN 9781118664285, https://doi.org/10.1029/GM055p0277, 1989.

Heimann, M., Esser, G., Haxeltine, A., Kaduk, J., Kicklighter, D. W., Knorr, W., Kohlmaier, G. H., McGuire, A. D., Melillo, J., Moore, B., Otto, R. D., Prentice, I. C., Sauf, W., Schloss, A., Sitch, S., Wittenberg, U., and Würth, G.: Evaluation of terrestrial carbon cycle models through simulations of the seasonal cycle of atmospheric CO_2: First results of a model intercomparison study, Global Biogeochem. Cy., 12, 1–24, https://doi.org/10.1029/97GB01936, 1998.

Hurtt, G. C., Chini, L., Sahajpal, R., Frolking, S., Bodirsky, B. L., Calvin, K., Doelman, J. C., Fisk, J., Fujimori, S., Klein Goldewijk, K., Hasegawa, T., Havlik, P., Heinimann, A., Humpenöder, F., Jungclaus, J., Kaplan, J. O., Kennedy, J., Krisztin, T., Lawrence, D., Lawrence, P., Ma, L., Mertz, O., Pongratz, J., Popp, A., Poulter, B., Riahi, K., Shevliakova, E., Stehfest, E., Thornton, P., Tubiello, F. N., van Vuuren, D. P., and Zhang, X.: Harmonization of global land use change and management for the period 850–2100 (LUH2) for CMIP6, Geosci. Model Dev., 13, 5425–5464, https://doi.org/10.5194/gmd-13-5425-2020, 2020.

Ito, A., Inatomi, M., Huntzinger, D. N., Schwalm, C., Michalak, A. M., Cook, R., King, A. W., Mao, J., Wei, Y., Post, W. M., Wang, W., Arain, M. A., Huang, S., Hayes, D. J., Ricciuto, D. M., Shi, X., Huang, M., Lei, H., Tian, H., Lu, C., Yang, J., Tao, B., Jain, A., Poulter, B., Peng, S., Ciais, P., Fisher, J. B., Parazoo, N., Schaefer, K., Peng, C., Zeng, N., and Zhao, F.: Decadal trends in the seasonal-cycle amplitude of terrestrial CO_2 exchange resulting from the ensemble of terrestrial biosphere models, Tellus B, 68, 28968, https://doi.org/10.3402/tellusb.v68.28968, 2016.

Jeltsch-Thömmes, A. and Joos, F.: Modeling the evolution of pulse-like perturbations in atmospheric carbon and carbon isotopes: the role of weathering–sedimentation imbalances, Clim. Past, 16, 423–451, https://doi.org/10.5194/cp-16-423-2020, 2020.

Jeltsch-Thömmes, A. and Joos, F.: Carbon Cycle Responses to Changes in Weathering and the Long-Term Fate of Stable Carbon Isotopes, Paleoceanogr. Paleocl., 38, e2022PA004577, https://doi.org/10.1029/2022PA004577, 2023.

Jin, Y., Keeling, R. F., Stephens, B. B., Long, M. C., Patra, P. K., Rödenbeck, C., Morgan, E. J., Kort, E. A., and Sweeney, C.: Improved atmospheric constraints on Southern Ocean CO_2 exchange, P. Natl. Acad. Sci., 121, e2309333121, https://doi.org/10.1073/pnas.2309333121, 2024.

Joos, F. and Bruno, M.: Long-term variability of the terrestrial and oceanic carbon sinks and the budgets of the carbon isotopes ^{13}C and ^{14}C, Global Biogeochem. Cy., 12, 277–295, https://doi.org/10.1029/98GB00746, 1998.

Joos, F., Hameau, A., Frölicher, T. L., and Stephenson, D. B.: Anthropogenic Attribution of the Increasing Seasonal Amplitude in Surface Ocean pCO_2, Geophys. Res. Lett., 50, e2023GL102857, https://doi.org/10.1029/2023GL102857, 2023.

Joos, F., Lienert, S., and Zaehle, S.: No increase is detected and modelled for the seasonal cycle amplitude of $\delta^{13}C$ of atmospheric carbon dioxide: scripts and data to prepare figures, Zenodo [data set], https://doi.org/10.5281/zenodo.14051464, 2024.

Kalnay, E., Kanamitsu, M., Kistler, R., Collins, W., Deaven, D., Gandin, L., Iredell, M., Saha, S., White, G., Woollen, J., Zhu, Y., Leetmaa, A., Reynolds, R., Chelliah, M., Ebisuzaki, W., Higgins, W., Janowiak, J., Mo, K. C., Ropelewski, C., Wang, J., Jenne, R., and Joseph, D.: The NCEP/NCAR 40-Year Reanalysis Project, B. Am. Meteorol. Soc., 77, 437–471, https://doi.org/10.1175/1520-0477(1996)077<0437:TNYRP>2.0.CO;2, 1996.

Kaminski, T., Heimann, M., and Giering, R.: A Global Scale Inversion of the Transport of CO_2 Based on a Matrix Representation of an Atmospheric Transport Model Derived by Its Adjoint, in: Air Pollution Modeling and Its Application XII, 247–255, Springer US, Boston, MA, https://doi.org/10.1007/978-1-4757-9128-0_26, 1998.

Kauwe, M. G., Medlyn, B. E., Zaehle, S., Walker, A. P., Dietze, M. C., Hickler, T., Jain, A. K., Luo, Y., Parton, W. J., Prentice, I. C., Smith, B., Thornton, P. E., Wang, S., Wang, Y.-P., Wårlind, D., Weng, E., Crous, K. Y., Ellsworth, D. S., Hanson, P. J., Kim, H.-S., Warren, J. M., Oren, R., and Norby, R. J.: Forest water use and water use efficiency at elevated CO_2: a model-data intercomparison at two contrasting temperate forest FACE sites, Glob. Change Biol., 19, 1759–1779, https://doi.org/10.1111/gcb.12164, 2013.

Keeling, C. D.: The Concentration and Isotopic Abundances of Carbon Dioxide in the Atmosphere, Tellus, 12, 200–203, https://doi.org/10.1111/j.2153-3490.1960.tb01300.x, 1960.

Keeling, C. D., Carter, A. F., and Mook, W. G.: Seasonal, latitudinal, and secular variations in the abundance and isotopic ratios of atmospheric CO_2: 2. Results from oceanographic cruises in the tropical Pacific Ocean, J. Geophys. Res.-Atmos., 89, 4615–4628, https://doi.org/10.1029/JD089iD03p04615, 1984.

Keeling, C. D., Bacastow, R. B., Carter, A. F., Piper, S. C., Whorf, T. P., Heimann, M., Mook, W. G., and Roeloffzen, H.: A three dimensional model of atmospheric CO_2 transport based on observed winds: 1. Analysis of Observational Data, in: Aspects of Climate Variability in the Pacific and the Western Americas, 165–236, American Geophysical Union (AGU), ISBN 9781118664285, https://doi.org/10.1029/GM055p0165, 1989.

Keeling, C. D., Chin, J. F. S., and Whorf, T. P.: Increased activity of northern vegetation inferred from atmospheric CO_2 measurements, Nature, 382, 146–149, https://doi.org/10.1038/382146a0, 1996.

Keeling, C. D., Piper, S. C., Bacastow, R. B., Wahlen, M., Whorf, T. P., Heimann, M., and Meijer, H. A.: Exchanges of atmospheric CO_2 and $^{13}CO_2$ with the terrestrial biosphere and oceans from 1978 to 2000. I. Global aspects, SIO Reference Series, No. 01-06, San Diego, p. 88, Scripps Institution of Oceanography [data sets], https://escholarship.org/uc/item/09v319r9 (last access: 23 December 2024), https://scrippsco2.ucsd.edu/data/atmospheric_co2 (last access: 17 April 2023), 2001.

Keeling, C. D., Piper, S. C., Bacastow, R. B., Wahlen, M., Whorf, T. P., Heimann, M., and Meijer, H. A.: Atmospheric CO_2 and $^{13}CO_2$ Exchange with the Terrestrial Biosphere and Oceans from 1978 to 2000: Observations and Carbon Cycle Implications, in: A History of Atmospheric CO_2 and Its Effects on Plants, Animals, and Ecosystems, edited by: Baldwin, I. T., Caldwell, M. M., Heldmaier, G., Jackson, R. B., Lange, O. L., Mooney, H. A., Schulze, E.-D., Sommer, U., Ehleringer, J. R., Denise Dearing, M., and Cerling, T. E., 83–113, Springer New York, New York, NY, ISBN 978-0-387-27048-7, https://doi.org/10.1007/0-387-27048-5_5, 2005.

Keeling, R. F., Graven, H. D., Welp, L. R., Resplandy, L., Bi, J., Piper, S. C., Sun, Y., Bollenbacher, A., and Meijer, H. A. J.: Atmospheric evidence for a global secular increase in carbon isotopic discrimination of land photosynthesis, P. Natl. Acad. Sci., 114, 10361–10366, https://doi.org/10.1073/pnas.1619240114, 2017.

Keenan, T. F., Hollinger, D. Y., Bohrer, G., Dragoni, D., Munger, J. W., Schmid, H. P., and Richardson, A. D.: Increase in forest water-use efficiency as atmospheric carbon dioxide concentrations rise, Nature, 499, 324–327, https://doi.org/10.1038/nature12291, 2013.

Keller, K. M., Joos, F., and Raible, C. C.: Time of emergence of trends in ocean biogeochemistry, Biogeosciences, 11, 3647–3659, https://doi.org/10.5194/bg-11-3647-2014, 2014.

Keller, K. M., Lienert, S., Bozbiyik, A., Stocker, T. F., Churakova (Sidorova), O. V., Frank, D. C., Klesse, S., Koven, C. D., Leuenberger, M., Riley, W. J., Saurer, M., Siegwolf, R., Weigt, R. B., and Joos, F.: 20th century changes in carbon isotopes and water-use efficiency: tree-ring-based evaluation of the CLM4.5 and LPX-Bern models, Biogeosciences, 14, 2641–2673, https://doi.org/10.5194/bg-14-2641-2017, 2017.

Knauer, J., Zaehle, S., Reichstein, M., Medlyn, B. E., Forkel, M., Hagemann, S., and Werner, C.: The response of ecosystem water-use efficiency to rising atmospheric CO_2 concentrations: sensitivity and large-scale biogeochemical implications, New Phytol., 213, 1654–1666, https://doi.org/10.1111/nph.14288, 2017.

Körner, C.: A matter of tree longevity, Science, 355, 130–131, https://doi.org/10.1126/science.aal2449, 2017.

Landschützer, P., Gruber, N., Bakker, D. C. E., and Schuster, U.: Recent variability of the global ocean carbon sink, Global Biogeochem. Cy., 28, 927–949, https://doi.org/10.1002/2014GB004853, 2014.

Lienert, S. and Joos, F.: A Bayesian ensemble data assimilation to constrain model parameters and land-use carbon emissions, Biogeosciences, 15, 2909–2930, https://doi.org/10.5194/bg-15-2909-2018, 2018.

Lloyd, J. and Farquhar, G.: ^{13}C discrimination during CO_2 assimilation by the terrestrial biosphere, Oecologia, 99, 201–215, https://doi.org/10.1007/BF00627732, 1994.

Long, M. C., Stephens, B. B., McKain, K., Sweeney, C., Keeling, R. F., Kort, E. A., Morgan, E. J., Bent, J. D., Chandra, N., Chevallier, F., Commane, R., Daube, B. C., Krummel, P. B., Loh, Z., Luijkx, I. T., Munro, D., Patra, P., Peters, W., Ramonet, M., Rödenbeck, C., Stavert, A., Tans, P., and Wofsy, S. C.: Strong Southern Ocean carbon uptake evident in airborne observations, Sci-

ence, 374, 1275–1280, https://doi.org/10.1126/science.abi4355, 2021.

Lueker, T., Keeling, R., Bollenbacher, A., Walker, S., Morgan, E., and Brooks, M.: Calibration Methodology for the Scripps $^{13}C/^{12}C$ and $^{18}O/^{16}O$ stable Isotope program 1992–2018, UC San Diego, Scripps Institution of Oceanography, https://escholarship.org/uc/item/4n93p288 (last access: 23 December 2024), p. 39, 2020.

Majkut, J. D., Carter, B. R., Frölicher, T. L., Dufour, C. O., Rodgers, K. B., and Sarmiento, J. L.: An observing system simulation for Southern Ocean carbon dioxide uptake, Philos. T. R. Soc. A, 372, 20130046, https://doi.org/10.1098/rsta.2013.0046, 2014.

Masarie, K. A., Peters, W., Jacobson, A. R., and Tans, P. P.: ObsPack: a framework for the preparation, delivery, and attribution of atmospheric greenhouse gas measurements, Earth Syst. Sci. Data, 6, 375–384, https://doi.org/10.5194/essd-6-375-2014, 2014.

Menviel, L., Mouchet, A., Meissner, K. J., Joos, F., and England, M. H.: Impact of oceanic circulation changes on atmospheric $\delta^{13}CO_2$, Global Biogeochem. Cy., 29, 1944–1961, https://doi.org/10.1002/2015GB005207, 2015.

Mook, W.: ^{13}C in atmospheric CO_2, Neth. J. Sea Res., 20, 211–223, https://doi.org/10.1016/0077-7579(86)90043-8, 1986.

Peng, S., Ciais, P., Chevallier, F., Peylin, P., Cadule, P., Sitch, S., Piao, S., Ahlström, A., Huntingford, C., Levy, P., Li, X., Liu, Y., Lomas, M., Poulter, B., Viovy, N., Wang, T., Wang, X., Zaehle, S., Zeng, N., Zhao, F., and Zhao, H.: Benchmarking the seasonal cycle of CO_2 fluxes simulated by terrestrial ecosystem models, Global Biogeochem. Cy., 29, 46–64, https://doi.org/10.1002/2014GB004931, 2015.

Peylin, P., Law, R. M., Gurney, K. R., Chevallier, F., Jacobson, A. R., Maki, T., Niwa, Y., Patra, P. K., Peters, W., Rayner, P. J., Rödenbeck, C., van der Laan-Luijkx, I. T., and Zhang, X.: Global atmospheric carbon budget: results from an ensemble of atmospheric CO_2 inversions, Biogeosciences, 10, 6699–6720, https://doi.org/10.5194/bg-10-6699-2013, 2013.

Peylin, P., Bacour, C., MacBean, N., Leonard, S., Rayner, P., Kuppel, S., Koffi, E., Kane, A., Maignan, F., Chevallier, F., Ciais, P., and Prunet, P.: A new stepwise carbon cycle data assimilation system using multiple data streams to constrain the simulated land surface carbon cycle, Geosci. Model Dev., 9, 3321–3346, https://doi.org/10.5194/gmd-9-3321-2016, 2016.

Peñuelas, J., Canadell, J. G., and Ogaya, R.: Increased water-use efficiency during the 20th century did not translate into enhanced tree growth, Global Ecol. Biogeogr., 20, 597–608, https://doi.org/10.1111/j.1466-8238.2010.00608.x, 2011.

Piao, S., Liu, Z., Wang, Y., Ciais, P., Yao, Y., Peng, S., Chevallier, F., Friedlingstein, P., Janssens, I. A., Peñuelas, J., Sitch, S., and Wang, T.: On the causes of trends in the seasonal amplitude of atmospheric CO_2, Glob. Change Biol., 24, 608–616, https://doi.org/10.1111/gcb.13909, 2018.

Quay, P. D., Sonnerup, R., Munro, D. R., and Sweeney, C.: Anthropogenic CO_2 accumulation and uptake rates in the Pacific Ocean based on changes in the $^{13}C/^{12}C$ of dissolved inorganic carbon, Global Biogeochem. Cy., 31, 59–80, https://doi.org/10.1002/2016GB005460, 2017.

Ritz, S. P., Stocker, T. F., Joos, F., Ritz, S. P., Stocker, T. F., and Joos, F.: A Coupled Dynamical Ocean–Energy Balance Atmosphere Model for Paleoclimate Studies, J. Climate, 24, 349–375, https://doi.org/10.1175/2010JCLI3351.1, 2011.

Saurer, M. and Voelker, S.: Intrinsic Water-Use Efficiency Derived from Stable Carbon Isotopes of Tree-Rings, 481–498, Springer International Publishing, Cham, ISBN 978-3-030-92698-4, https://doi.org/10.1007/978-3-030-92698-4_17, 2022.

Saurer, M., Spahni, R., Frank, D. C., Joos, F., Leuenberger, M., Loader, N. J., McCarroll, D., Gagen, M., Poulter, B., Siegwolf, R. T., Andreu-Hayles, L., Boettger, T., Dorado Liñán, I., Fairchild, I. J., Friedrich, M., Gutierrez, E., Haupt, M., Hilasvuori, E., Heinrich, I., Helle, G., Grudd, H., Jalkanen, R., Levanič, T., Linderholm, H. W., Robertson, I., Sonninen, E., Treydte, K., Waterhouse, J. S., Woodley, E. J., Wynn, P. M., and Young, G. H.: Spatial variability and temporal trends in water-use efficiency of European forests, Glob. Change Biol., 20, 3700–3712, https://doi.org/10.1111/gcb.12717, 2014.

Scholze, M., Kaplan, J. O., Knorr, W., and Heimann, M.: Climate and interannual variability of the atmosphere-biosphere $^{13}CO_2$ flux, Geophys. Res. Lett., 30, 1–4, https://doi.org/10.1029/2002GL015631, 2003.

Scholze, M., Ciais, P., and Heimann, M.: Modeling terrestrial ^{13}C cycling: Climate, land use and fire, Global Biogeochem. Cy., 22, 1–13, https://doi.org/10.1029/2006GB002899, 2008.

Schürmann, G. J., Kaminski, T., Köstler, C., Carvalhais, N., Voßbeck, M., Kattge, J., Giering, R., Rödenbeck, C., Heimann, M., and Zaehle, S.: Constraining a land-surface model with multiple observations by application of the MPI-Carbon Cycle Data Assimilation System V1.0, Geosci. Model Dev., 9, 2999–3026, https://doi.org/10.5194/gmd-9-2999-2016, 2016.

Sitch, S., Smith, B., Prentice, I. C., Arneth, A., Bondeau, A., Cramer, W., Kaplan, J. O., Levis, S., Lucht, W., Sykes, M. T., Thonicke, K., and Venevsky, S.: Evaluation of ecosystem dynamics, plant geography and terrestrial carbon cycling in the LPJ dynamic global vegetation model, Glob. Change Biol., 9, 161–185, https://doi.org/10.1046/j.1365-2486.2003.00569.x, 2003.

Still, C. J., Berry, J. A., Collatz, G. J., and DeFries, R. S.: Global distribution of C_3 and C_4 vegetation: Carbon cycle implications, Global Biogeochem. Cy., 17, 6-1–6-14, https://doi.org/10.1029/2001GB001807, 2003.

Stocker, B. D., Spahni, R., and Joos, F.: DYPTOP: a cost-efficient TOPMODEL implementation to simulate sub-grid spatio-temporal dynamics of global wetlands and peatlands, Geosci. Model Dev., 7, 3089–3110, https://doi.org/10.5194/gmd-7-3089-2014, 2014.

Strassmann, K. M., Joos, F., and Fischer, G.: Simulating effects of land use changes on carbon fluxes: past contributions to atmospheric CO_2 increases and future commitments due to losses of terrestrial sink capacity, Tellus B, 60, 583–603, 2008.

Takahashi, T., Sutherland, S. C., Wanninkhof, R., Sweeney, C., Feely, R. A., Chipman, D. W., Hales, B., Friederich, G., Chavez, F., Sabine, C., Watson, A., Bakker, D. C., Schuster, U., Metzl, N., Yoshikawa-Inoue, H., Ishii, M., Midorikawa, T., Nojiri, Y., Körtzinger, A., Steinhoff, T., Hoppema, M., Olafsson, J., Arnarson, T. S., Tilbrook, B., Johannessen, T., Olsen, A., Bellerby, R., Wong, C., Delille, B., Bates, N., and de Baar, H. J.: Climatological mean and decadal change in surface ocean pCO_2, and net sea–air CO_2 flux over the global oceans, Deep-Sea Res. Pt. II, 56, 554–577, https://doi.org/10.1016/j.dsr2.2008.12.009, 2009.

Tans, P. P., Berry, J. A., and Keeling, R. F.: Oceanic $^{13}C/^{12}C$ observations: A new window on ocean CO_2 uptake, Global Biogeochem. Cy., 7, 353–368, https://doi.org/10.1029/93GB00053, 1993.

Tian, H., Yang, J., Lu, C., Xu, R., Canadell, J. G., Jackson, R. B., Arneth, A., Chang, J., Chen, G., Ciais, P., Gerber, S., Ito, A., Huang, Y., Joos, F., Lienert, S., Messina, P., Olin, S., Pan, S., Peng, C., Saikawa, E., Thompson, R. L., Vuichard, N., Winiwarter, W., Zaehle, S., Zhang, B., Zhang, K., and Zhu, Q.: The Global N_2O Model Intercomparison Project, B. Am. Meteorol. Soc., 99, 1231–1251, https://doi.org/10.1175/BAMS-D-17-0212.1, 2018.

van der Velde, I. R., Miller, J. B., Schaefer, K., Masarie, K. A., Denning, S., White, J. W. C., Tans, P. P., Krol, M. C., and Peters, W.: Biosphere model simulations of interannual variability in terrestrial $^{13}C/^{12}C$ exchange, Global Biogeochem. Cy., 27, 637–649, https://doi.org/10.1002/gbc.20048, 2013.

van der Velde, I. R., Miller, J. B., van der Molen, M. K., Tans, P. P., Vaughn, B. H., White, J. W. C., Schaefer, K., and Peters, W.: The CarbonTracker Data Assimilation System for CO_2 and $\delta^{13}C$ (CTDAS-C13 v1.0): retrieving information on land–atmosphere exchange processes, Geosci. Model Dev., 11, 283–304, https://doi.org/10.5194/gmd-11-283-2018, 2018.

Voelker, S. L., Brooks, J. R., Meinzer, F. C., Anderson, R., Bader, M. K.-F., Battipaglia, G., Becklin, K. M., Beerling, D., Bert, D., Betancourt, J. L., Dawson, T. E., Domec, J.-C., Guyette, R. P., Körner, C., Leavitt, S. W., Linder, S., Marshall, J. D., Mildner, M., Ogée, J., Panyushkina, I., Plumpton, H. J., Pregitzer, K. S., Saurer, M., Smith, A. R., Siegwolf, R. T. W., Stambaugh, M. C., Talhelm, A. F., Tardif, J. C., Van de Water, P. K., Ward, J. K., and Wingate, L.: A dynamic leaf gas-exchange strategy is conserved in woody plants under changing ambient CO_2: evidence from carbon isotope discrimination in paleo and CO_2 enrichment studies, Glob. Change Biol., 22, 889–902, https://doi.org/10.1111/gcb.13102, 2016.

Walker, A. P., De Kauwe, M. G., Bastos, A., Belmecheri, S., Georgiou, K., Keeling, R. F., McMahon, S. M., Medlyn, B. E., Moore, D. J., Norby, R. J., Zaehle, S., Anderson-Teixeira, K. J., Battipaglia, G., Brienen, R. J., Cabugao, K. G., Cailleret, M., Campbell, E., Canadell, J. G., Ciais, P., Craig, M. E., Ellsworth, D. S., Farquhar, G. D., Fatichi, S., Fisher, J. B., Frank, D. C., Graven, H., Gu, L., Haverd, V., Heilman, K., Heimann, M., Hungate, B. A., Iversen, C. M., Joos, F., Jiang, M., Keenan, T. F., Knauer, J., Körner, C., Leshyk, V. O., Leuzinger, S., Liu, Y., MacBean, N., Malhi, Y., McVicar, T. R., Penuelas, J., Pongratz, J., Powell, A. S., Riutta, T., Sabot, M. E., Schleucher, J., Sitch, S., Smith, W. K., Sulman, B., Taylor, B., Terrer, C., Torn, M. S., Treseder, K. K., Trugman, A. T., Trumbore, S. E., van Mantgem, P. J., Voelker, S. L., Whelan, M. E., and Zuidema, P. A.: Integrating the evidence for a terrestrial carbon sink caused by increasing atmospheric CO_2, New Phytol., 229, 2413–2445, https://doi.org/10.1111/nph.16866, 2021.

Wang, S., Zhang, Y., Ju, W., Chen, J. M., Ciais, P., Cescatti, A., Sardans, J., Janssens, I. A., Wu, M., Berry, J. A., Campbell, E., Fernández-Martínez, M., Alkama, R., Sitch, S., Friedlingstein, P., Smith, W. K., Yuan, W., He, W., Lombardozzi, D., Kautz, M., Zhu, D., Lienert, S., Kato, E., Poulter, B., Sanders, T. G. M., Krüger, I., Wang, R., Zeng, N., Tian, H., Vuichard, N., Jain, A. K., Wiltshire, A., Haverd, V., Goll, D. S., and Peñuelas, J.: Recent global decline of CO_2 fertilization effects on vegetation photosynthesis, Science, 370, 1295–1300, https://doi.org/10.1126/science.abb7772, 2020.

Wania, R., Ross, I., and Prentice, I. C.: Integrating peatlands and permafrost into a dynamic global vegetation model: 1. Evaluation and sensitivity of physical land surface processes, Global Biogeochem. Cy., 23, 1–19, https://doi.org/10.1029/2008GB003412, 2009a.

Wania, R., Ross, I., and Prentice, I. C.: Integrating peatlands and permafrost into a dynamic global vegetation model: 2. Evaluation and sensitivity of vegetation and carbon cycle processes, Global Biogeochem. Cy., 23, 1–15, https://doi.org/10.1029/2008GB003413, 2009b.

Welch, B. L.: The Generalization of "Student's" Problem when Several Different Population Variances are Involved, Biometrika, 34, 28–35, https://doi.org/10.2307/2332510, 1947.

Xu-Ri and Prentice, I. C.: Terrestrial nitrogen cycle simulation with a dynamic global vegetation model, Glob. Change Biol., 14, 1745–1764, https://doi.org/10.1111/j.1365-2486.2008.01625.x, 2008.